

# Chapter 10

## LONG RANGE INTERACTIONS IN 2D SYSTEMS

### 10.1. Dipole–Dipole Interaction in 2D Systems

The study of 2D systems with dipole–dipole interaction is of interest for both theoretical and experimental reasons. The most intriguing question to which the statistical physics tries to give answer is: How the long range nature of the dipolar interaction affects the thermodynamic properties of a magnetic system? In other words, the LRO of a magnetic system can be recovered by the dipolar interaction in 2D system with continuous symmetry for which the Mermin and Wagner theorem<sup>22</sup> rules out any LRO in presence of short range interactions. Even though the 2D spin systems with continuous symmetry and short range interaction do not support LRO, different scenarios are found for the 2D Heisenberg model in which the spins are three-component vectors and the 2D planar rotator model in which the spins are two-component vectors. Indeed, the 2D Heisenberg model with NN exchange interaction is paramagnetic at any finite temperature while the 2D planar rotator model with NN exchange interaction shows<sup>89</sup> a Berezinskii–Kosterlitz–Thouless (BKT) phase characterized by divergent susceptibility and algebraic decaying of the spin–spin correlation function at temperatures<sup>90</sup>  $T < T_{KT} = (0.895 \pm 0.005)J$ . How is the BKT phase modified in replacing the NN exchange interaction by a long range interaction? When the spin–spin interaction is an *isotropic* long range interaction, for instance, assuming an exchange coupling decaying as  $\frac{1}{r^3}$  where  $r$  is the spin–spin distance, a variety of different behaviours are expected. A ferromagnetic long range interaction supports LRO as shown by renormalization group (RG) analysis<sup>91</sup> and confirmed by Monte Carlo (MC) simulation.<sup>92</sup> On the contrary, an antiferromagnetic long range coupling decaying with the same power law  $\frac{1}{r^3}$  is expected to be unable to support LRO on the basis of MC simulation and confirmed by analytic calculations performed using the harmonic spin wave approximation.<sup>93</sup> What happens when the long range interaction is an *anisotropic* interaction as the dipole–dipole one? The ground state of a SQ planar rotator model with pure dipole–dipole interaction was found<sup>94</sup> to be infinitely many-fold degenerate. In particular, it consists of four sublattices<sup>95,96</sup> where the magnetic moments of each sublattice make an angle  $\alpha$ ,  $-\alpha$ ,  $\pi + \alpha$  and  $\pi - \alpha$ , with the  $x$ -axis,  $\alpha$  being

arbitrary. Two configurations of this many-fold correspond to helix phases: indeed, the ground state with  $\alpha = 0$  is recovered by a *columnar* phase with  $\mathbf{Q} = \frac{2\pi}{a}(0, \frac{1}{2})$  and the ground state with  $\alpha = \frac{\pi}{2}$  is recovered by another columnar configuration with  $\mathbf{Q} = \frac{2\pi}{a}(\frac{1}{2}, 0)$ . When the ground state is characterized by a continuous degeneracy, the harmonic spin wave approximation which is usually a reliable low temperature approach leads to a divergent mean-square angular displacement that destroys the LRO. However, the free energy obtained from the harmonic spin wave approximation is a function of the angle  $\alpha$  so that its minimization selects a well-defined configuration,<sup>95,96</sup> lifting the continuous degeneracy at finite temperature and recovering the LRO. Such a phenomenology is called<sup>97</sup> *order by thermal disorder*. The recovering of the LRO cannot be obtained using the harmonic spin waves but one must use the *renormalized* spin waves as it will be illustrated in the next section.

The main numerical investigation on the statistical physics of the planar rotator model is obtained from the MC simulation. For a comprehensive book on this argument, we point out *A Guide to Monte Carlo Simulations in Statistical Physics* by David P. Landau and Kurt Binder (Cambridge University Press). In the next section, the analytic result obtained from the renormalized spin wave theory and the numerical result obtained from MC simulation will be compared at low temperature where the two approaches overlap.

Another important motivation to study 2D systems with dipole–dipole interaction comes from the technological interest in the ultrathin films (1–10 atomic layers) whose magnetization perpendicular to the film surface consists of *stripes* of spins aligned up and down. These unexpected configurations have been seen in ultrathin films<sup>98</sup> of Fe (2.5–3.5 atomic layers) grown on the (1, 0, 0) surface of Cu and<sup>99</sup> Co (3–4.5 atomic layers) grown on the surface (1, 1, 1) of Au. These ultrathin films can be represented by 2D Ising models with both short range exchange and long range dipolar interactions. The choice of the Ising model, in which the spins are one-component vectors, is justified by the strong anisotropy that favours the alignment of the magnetic moments perpendicular to the surface. Indeed, the experiments on the ultrathin films show a reorientation of the magnetization from the direction perpendicular to the surface to a direction parallel to the surface, increasing the number of layers, that is going from 2D to 3D systems. In Section 10.3, we will show the existence of stripes and checkerboard configurations by simply considering a 2D Ising model with NN ferromagnetic and dipole–dipole interaction and changing the weight of the short and long range interactions.

We conclude this section by giving the ground-state energy of a 2D system with dipole–dipole interaction and extending the Ewald’s method of Section 9.2 to the 2D case. The key point is to change the 3D theta-function transformation given by Eq. (9.2.4) into the corresponding 2D theta-function transformation

$$\sum_l z^2 e^{i\mathbf{Q} \cdot \mathbf{r}_l} e^{-r_l^2 z^2} = \rho\pi \sum_l e^{-\frac{(\mathbf{G}_l + \mathbf{Q})^2}{4z^2}}. \quad (10.1.1)$$

By means of Eq. (10.1.1), Eq. (9.2.1) becomes

$$\sum_{l \neq 0} \frac{e^{i\mathbf{Q} \cdot \mathbf{r}_l}}{r_l^3} = -\frac{4\eta^3}{3\sqrt{\pi}} + 4\rho\eta\sqrt{\pi} \sum_l f_A \left( \frac{|\mathbf{G}_l + \mathbf{Q}|}{2\eta} \right) + \frac{2\eta^3}{\sqrt{\pi}} \sum_{l \neq 0} e^{i\mathbf{Q} \cdot \mathbf{r}_l} f_B(\eta r_l) \quad (10.1.2)$$

where

$$f_A(x) = \frac{x}{2} \int_{x^2}^{\infty} dz \frac{e^{-z}}{z^{3/2}} = e^{-x^2} - \sqrt{\pi} x \operatorname{erfc}(x) \quad (10.1.3)$$

and  $f_B(x)$  is given by Eq. (9.2.8). Using again Eq. (10.1.1), the sum (9.2.18) becomes

$$\begin{aligned} \sum_{l \neq 0} \frac{e^{i\mathbf{Q} \cdot \mathbf{r}_l}}{r_l^5} r_l^\alpha r_l^\beta &= \frac{4}{3} \rho \eta \sqrt{\pi} \delta_{\alpha, \beta} \sum_l f_A \left( \frac{|\mathbf{G}_l + \mathbf{Q}|}{2\eta} \right) \\ &\quad - \frac{2}{3} \rho \pi \sum_l \frac{(\mathbf{G}_l + \mathbf{Q})_\alpha (\mathbf{G}_l + \mathbf{Q})_\beta}{|\mathbf{G}_l + \mathbf{Q}|} \operatorname{erfc} \left( \frac{|\mathbf{G}_l + \mathbf{Q}|}{2\eta} \right) \\ &\quad + \frac{4\eta^5}{3\sqrt{\pi}} \sum_{l \neq 0} r_l^\alpha r_l^\beta e^{i\mathbf{Q} \cdot \mathbf{r}_l} f_D(\eta r_l) \end{aligned} \quad (10.1.4)$$

where  $f_D(x)$  is given by Eq. (9.2.16) and  $\alpha, \beta = x, y$ . Replacing Eqs. (10.1.2) and (10.1.4) into Eq. (9.2.19), the 2D dipolar sums become

$$\begin{aligned} D_\infty^{\alpha\beta}(\mathbf{Q}) &= -2\pi\rho \sum_l \frac{(\mathbf{G}_l + \mathbf{Q})_\alpha (\mathbf{G}_l + \mathbf{Q})_\beta}{|\mathbf{G}_l + \mathbf{Q}|} \operatorname{erfc} \left( \frac{|\mathbf{G}_l + \mathbf{Q}|}{2\eta} \right) \\ &\quad + \frac{4\eta^5}{\sqrt{\pi}} \sum_{l \neq 0} r_l^\alpha r_l^\beta e^{i\mathbf{Q} \cdot \mathbf{r}_l} f_D(\eta r_l) + \frac{2\eta^3}{\sqrt{\pi}} \delta_{\alpha, \beta} \left[ \frac{2}{3} - \sum_{l \neq 0} e^{i\mathbf{Q} \cdot \mathbf{r}_l} f_B(\eta r_l) \right]. \end{aligned} \quad (10.1.5)$$

In the limit  $\mathbf{Q} \rightarrow 0$ , one has

$$\lim_{\mathbf{Q} \rightarrow 0} D_\infty^{\alpha\beta}(\mathbf{Q}) = \delta_{\alpha, \beta} d_\alpha \quad (10.1.6)$$

where

$$d_\alpha = \frac{4\eta^3}{3\sqrt{\pi}} - 2\pi\rho \sum_{l \neq 0} \frac{(G_l^\alpha)^2}{G_l} \operatorname{erfc} \left( \frac{G_l}{2\eta} \right) + \frac{2\eta^3}{\sqrt{\pi}} \sum_{l \neq 0} [2(\eta r_l^\alpha)^2 f_D(\eta r_l) - f_B(\eta r_l)]. \quad (10.1.7)$$

For a SQ lattice, one has

$$\sum_{l \neq 0} \frac{(G_l^\alpha)^2}{G_l} \operatorname{erfc} \left( \frac{G_l}{2\eta} \right) = \frac{1}{2} \sum_{l \neq 0} G_l \operatorname{erfc} \left( \frac{G_l}{2\eta} \right) \quad (10.1.8)$$

and

$$\sum_{l \neq 0} (\eta r_l^\alpha)^2 f_D(\eta r_l) = \frac{1}{2} \sum_{l \neq 0} (\eta r_l)^2 f_D(\eta r_l), \quad (10.1.9)$$

so that

$$\begin{aligned} d_x = d_y &= \frac{4\eta^3}{3\sqrt{\pi}} - \frac{\pi}{a^2} \sum_{l \neq 0} G_l \operatorname{erfc}\left(\frac{G_l}{2\eta}\right) \\ &\quad + \frac{2\eta^3}{\sqrt{\pi}} \sum_{l \neq 0} \left[ \frac{1 + 2(\eta r_l)^2}{2(\eta r_l)^2} e^{-\eta^2 r_l^2} + \frac{\sqrt{\pi}}{4(\eta r_l)^3} \operatorname{erfc}(\eta r_l) \right]. \\ &= \frac{4.5168108}{a^3}. \end{aligned} \quad (10.1.10)$$

The numerical value is evaluated by limiting the sums to  $-5 < l_1, l_2 < 5$  and assuming  $\eta = \frac{2}{a}$ . As in the 3D case, the numerical accuracy is within  $10^{-10}$ . In 2D, the finite size effect is not as important as in 3D. Indeed, for a sample made up of a circle of radius  $R$  ( $S = \pi R^2$ ), the dipolar sums are given by

$$D_S^{\alpha\beta}(\mathbf{Q}) = D_\infty^{\alpha\beta}(\mathbf{Q}) - D_{\infty-S}^{\alpha\beta}(\mathbf{Q}) \quad (10.1.11)$$

where, choosing polar coordinates such that  $\mathbf{Q} = Q(\cos \phi, \sin \phi)$  and  $\mathbf{r} = r[\cos(\phi + \theta), \sin(\phi + \theta)]$ , one has  $\mathbf{Q} \cdot \mathbf{r} = Qr \cos \theta$  and

$$D_{\infty-S}^{xx}(\mathbf{Q}) = Q \frac{\pi}{a^2} \int_{QR}^{\infty} \frac{dx}{x^2} [J_0(x) - 3J_2(x) \cos 2\phi], \quad (10.1.12)$$

$$D_{\infty-S}^{yy}(\mathbf{Q}) = Q \frac{\pi}{a^2} \int_{QR}^{\infty} \frac{dx}{x^2} [J_0(x) + 3J_2(x) \cos 2\phi] \quad (10.1.13)$$

and

$$D_{\infty-S}^{xy}(\mathbf{Q}) = -Q \frac{3\pi}{a^2} \sin 2\phi \int_{QR}^{\infty} \frac{dx}{x^2} J_2(x) \quad (10.1.14)$$

where  $J_n(x)$  are the Bessel functions of integer order<sup>3</sup> coming from the integration over  $\theta$  and  $x = Qr$ . For  $x \rightarrow 0$ , one has

$$J_0(x) = 1 - \frac{1}{4}x^2 + \frac{1}{64}x^4 + \dots \quad (10.1.15)$$

and

$$J_2(x) = \frac{1}{8}x^2 - \frac{1}{96}x^4 + \dots \quad (10.1.16)$$

so that the integrals occurring in Eqs. (10.1.12) and (10.1.13) are singular for  $Q \rightarrow 0$  while the integral occurring in Eq. (10.1.14) is finite for  $Q = 0$ . Then

$$\lim_{Q \rightarrow 0} D_{\infty-S}^{xx}(\mathbf{Q}) = \lim_{Q \rightarrow 0} D_{\infty-S}^{yy}(\mathbf{Q}) = \frac{\pi}{a^2 R} \quad (10.1.17)$$

and

$$\lim_{Q \rightarrow 0} D_{\infty-S}^{xy}(\mathbf{Q}) = 0. \quad (10.1.18)$$

Equation (10.1.17) shows that the 2D dipolar sums for finite samples differ from the corresponding sums for infinite samples by terms of order  $\frac{a}{R}$ . For macroscopic

Table 10.1. Dipolar sums for SQ lattice for selected values of the wavevector  $\mathbf{Q} = (q_1, q_2)$ .

$\mathbf{Q} = \frac{2\pi}{a} (q_1, q_2)$	$a^3 D^{xx}(\mathbf{Q})$	$a^3 D^{yy}(\mathbf{Q})$	$a^3 D^{zz}(\mathbf{Q})$
$(0, 0)$	4.5168108416	4.5168108416	-9.0336216831
$(\frac{1}{2}, 0)$	-6.0343351486	5.0988729940	0.9354621546
$(0, \frac{1}{2})$	5.0988729940	-6.0343351486	0.9354621546
$(\frac{1}{2}, \frac{1}{2})$	-1.3229432662	-1.3229432662	2.6458865323

samples, these corrections are of the order  $10^{-7}$  or less. For this reason, in the following, we will ignore any distinction between finite and infinite systems and suppress any subscript in the dipolar sums. In Table 10.1, we give the dipolar sums  $D^{\alpha\alpha}(\mathbf{Q})$  for a SQ lattice obtained from Eq. (10.1.5) for selected values of  $\mathbf{Q} = \frac{2\pi}{a}(q_1, q_2)$ . The last column is obtained from the first and second ones by means of the sum rule

$$D^{xx}(\mathbf{Q}) + D^{yy}(\mathbf{Q}) + D^{zz}(\mathbf{Q}) = 0. \quad (10.1.19)$$

As one can see from Table 10.1, the ground-state energy of a planar rotator model is

$$E_0^x\left(0, \frac{1}{2}\right) = E_0^y\left(\frac{1}{2}, 0\right) = -5.0988730 \frac{(\mu S)^2}{2a^3} N, \quad (10.1.20)$$

where the superscripts  $x$  and  $y$  indicate the spin direction. The corresponding configurations are *columnar* configurations characterized by alternating ferromagnetic rows or columns with the spins directed along the ferromagnetic chains. The dipolar sum for a 2D Ising model with the spins directed along the  $z$ -axis assumed to be perpendicular to the plane is

$$D^{zz}(\mathbf{Q}) = - \sum_{l \neq 0} \frac{e^{i\mathbf{Q} \cdot \mathbf{r}_l}}{r_l^3}. \quad (10.1.21)$$

The last column of Table 10.1 gives the values of  $D^{zz}(\mathbf{Q})$  for selected wavevectors  $\mathbf{Q}$ . The ground state of the 2D Ising model with pure dipole-dipole interaction and spins perpendicular to the plane is

$$E_0^z\left(\frac{1}{2}, \frac{1}{2}\right) = -2.6458865 \frac{(\mu S)^2}{2a^3} N \quad (10.1.22)$$

corresponding to a Néel antiferromagnetic configuration.

## 10.2. Planar Rotator Model with Long Range Interactions

The Hamiltonian of the planar rotator model with pure dipolar interaction reads

$$\mathcal{H} = -\frac{1}{2}\mu^2 \sum_i \sum_{\mathbf{r} \neq 0} \sum_{\alpha\beta} \frac{1}{r^3} \left( 3 \frac{r^\alpha r^\beta}{r^2} - \delta_{\alpha,\beta} \right) S_i^\alpha S_{i+\mathbf{r}}^\beta, \quad (10.2.1)$$

where  $\mu$  is the magnetic moment;  $\alpha, \beta = x, y$  label the two spin components;  $i$  labels the  $N$  sites of a SQ lattice;  $\mathbf{r} = a(l_1 \mathbf{u}_x + l_2 \mathbf{u}_y)$ , with  $l_1, l_2$  integers, is the

generic lattice vector;  $a$  is the lattice constant. The ground-state spin configuration selected by thermal fluctuations is a columnar configuration<sup>95,96</sup> whose energy is given by Eq. (10.1.20). To study the elementary excitations, we assume that the spin components of the planar rotator model are

$$S_i^x = S \cos(\mathbf{Q} \cdot \mathbf{r}_i + \psi_i), \quad S_i^y = S \sin(\mathbf{Q} \cdot \mathbf{r}_i + \psi_i), \quad (10.2.2)$$

where  $\mathbf{Q} = \frac{2\pi}{a}(0, \frac{1}{2})$  is the order wavevector characterizing the columnar configuration and  $\psi_i$  is the angular displacement from the ground-state configuration at site  $i$ . The elementary excitations correspond to small oscillations around the ground-state configuration so that when we expand Hamiltonian (10.2.1) in powers of the angular displacements  $\psi_i$ , keeping contributions up to fourth order, and use the Fourier transforms of the angular displacements

$$\psi_i = \frac{1}{\sqrt{N}} \sum_{\mathbf{q}} \psi_{\mathbf{q}} e^{i\mathbf{q} \cdot \mathbf{r}_i}, \quad (10.2.3)$$

the Hamiltonian (10.2.1) becomes

$$\mathcal{H} = E_0 + \mathcal{H}_2 + \mathcal{H}_3 + \mathcal{H}_4 + \dots \quad (10.2.4)$$

where

$$E_0 = -\frac{1}{2}N\mu^2 S^2 D^{xx}(\mathbf{Q}) = -5.0988730 \frac{(\mu S)^2}{2a^3} N, \quad (10.2.5)$$

$$\mathcal{H}_2 = \frac{1}{2}\mu^2 S^2 \sum_{\mathbf{q}} [D^{xx}(\mathbf{Q}) - D^{yy}(\mathbf{Q} - \mathbf{q})] \psi_{\mathbf{q}} \psi_{-\mathbf{q}}, \quad (10.2.6)$$

$$\mathcal{H}_3 = -\frac{1}{2}\mu^2 S^2 \frac{1}{\sqrt{N}} \sum_{\mathbf{q}_1, \mathbf{q}_2, \mathbf{q}_3} \delta_{\mathbf{q}_1 + \mathbf{q}_2 + \mathbf{q}_3, 0} D^{xy}(\mathbf{Q} - \mathbf{q}_1) \psi_{\mathbf{q}_1} \psi_{\mathbf{q}_2} \psi_{\mathbf{q}_3}, \quad (10.2.7)$$

$$\begin{aligned} \mathcal{H}_4 = & -\frac{1}{24}\mu^2 S^2 \frac{1}{N} \sum_{\mathbf{q}_1, \mathbf{q}_2, \mathbf{q}_3, \mathbf{q}_4} \delta_{\mathbf{q}_1 + \mathbf{q}_2 + \mathbf{q}_3 + \mathbf{q}_4, 0} [D^{xx}(\mathbf{Q}) + 3D^{xx}(\mathbf{Q} - \mathbf{q}_1 - \mathbf{q}_2) \\ & - 4D^{yy}(\mathbf{Q} - \mathbf{q}_1)] \psi_{\mathbf{q}_1} \psi_{\mathbf{q}_2} \psi_{\mathbf{q}_3} \psi_{\mathbf{q}_4}. \end{aligned} \quad (10.2.8)$$

The harmonic spin wave spectrum is

$$\hbar\omega_2(\mathbf{q}) = \frac{\mu^2 S^2}{2a^3} \epsilon_{\mathbf{q}} \quad (10.2.9)$$

where

$$\epsilon_{\mathbf{q}} = a^3 [D^{xx}(\mathbf{Q}) - D^{yy}(\mathbf{Q} - \mathbf{q})]. \quad (10.2.10)$$

Note that the spectrum (10.2.9) vanishes at  $\mathbf{q}_0 = \frac{2\pi}{a}(\frac{1}{2}, \frac{1}{2})$  as one can see from Table 10.1. Indeed, for  $\mathbf{q} = \mathbf{q}_0$ , one has  $\mathbf{Q} - \mathbf{q}_0 = -\frac{2\pi}{a}(\frac{1}{2}, 0) \equiv -\mathbf{Q}'$  and from Table 10.1, one sees that  $a^3 D^{xx}(\mathbf{Q}) = a^3 D^{yy}(\mathbf{Q}') = 5.0988730$ . The order parameter

in harmonic approximation is zero for any finite temperature. Indeed,

$$\langle \psi_i^2 \rangle = \frac{1}{N} \sum_{\mathbf{q}} \langle \psi_{\mathbf{q}} \psi_{-\mathbf{q}} \rangle_0 = \frac{1}{N} \sum_{\mathbf{q}} \frac{\int_0^\infty d|\psi_{\mathbf{q}}| |\psi_{\mathbf{q}}|^2 e^{-\beta \hbar \omega_2(\mathbf{q}) |\psi_{\mathbf{q}}|^2}}{\int_0^\infty d|\psi_{\mathbf{q}}| e^{-\beta \hbar \omega_2(\mathbf{q}) |\psi_{\mathbf{q}}|^2}} = \frac{1}{N} \sum_{\mathbf{q}} \frac{t}{\epsilon_{\mathbf{q}}} \quad (10.2.11)$$

where

$$t = \frac{k_B T a^3}{\mu^2 S^2} \quad (10.2.12)$$

is a reduced temperature. The expansion of  $\epsilon_{\mathbf{q}}$  about  $\mathbf{q}_0$  gives

$$\epsilon_{\mathbf{q} \rightarrow \mathbf{q}_0} = 0.14474(aq_x - \pi)^2 + 1.7873(aq_y - \pi)^2. \quad (10.2.13)$$

Equation (10.2.13) is obtained using the series expansions of Eq. (10.1.5) about  $\mathbf{Q}' = (\frac{1}{2}, 0)$  for  $\alpha = \beta = y$ . The vanishing of the harmonic spin wave spectrum about  $\mathbf{q}_0$  leads to a logarithmic divergence of the sum (10.2.11) so that  $\langle \psi_i^2 \rangle \rightarrow \infty$  and the order parameter

$$\langle \cos \psi_i \rangle = \cos \mathbf{Q} \cdot \mathbf{r}_i e^{-\frac{1}{2} \langle \psi_i^2 \rangle} \quad (10.2.14)$$

goes to zero at any finite temperature. This event claims for a more accurate treatment of the elementary excitations spectrum going beyond the harmonic approximation. To this end, we make use of the “classical” equivalent of the Dyson’s equation of Section 3.5. To obtain the perturbation expansion of the classical propagator (cumulant expansion), we split the Hamiltonian (10.2.4) in two parts: the unperturbed (harmonic) Hamiltonian  $\mathcal{H}_2$  and the perturbation  $V = \mathcal{H} - \mathcal{H}_2$ . Then we expand the exponential function containing  $V$  in a power series of  $\beta V$ . By doing so, one obtains

$$\langle \psi_{\mathbf{q}} \psi_{-\mathbf{q}} \rangle = \frac{\sum_{n=0}^{\infty} (-1)^n \frac{\beta^n}{n!} \langle \psi_{\mathbf{q}} \psi_{-\mathbf{q}} V^n \rangle_0}{\sum_{n=0}^{\infty} (-1)^n \frac{\beta^n}{n!} \langle V^n \rangle_0} \quad (10.2.15)$$

where the subscript 0 means a thermal average over the ensemble with the Hamiltonian  $\mathcal{H}_2$ . By means of the linked cluster theorem and the diagrams expansion of Chapter 4, Eq. (10.2.15) becomes

$$\langle \psi_{\mathbf{q}} \psi_{-\mathbf{q}} \rangle = \sum_{n=0}^{\infty} (-1)^n \frac{\beta^n}{n!} \langle \psi_{\mathbf{q}} \psi_{-\mathbf{q}} V^n \rangle_0^c \quad (10.2.16)$$

where the superscript  $c$  means “connected” diagrams. Restricting to the second-order perturbation theory, the expansion (10.2.16) for the Hamiltonian (10.2.4) reads

$$\langle \psi_{\mathbf{q}} \psi_{-\mathbf{q}} \rangle = \langle \psi_{\mathbf{q}} \psi_{-\mathbf{q}} \rangle_0 - \beta \langle \psi_{\mathbf{q}} \psi_{-\mathbf{q}} \mathcal{H}_4 \rangle_0^c + \frac{1}{2} \beta^2 \langle \psi_{\mathbf{q}} \psi_{-\mathbf{q}} \mathcal{H}_3^2 \rangle_0^c \quad (10.2.17)$$

where

$$\langle \psi_{\mathbf{q}} \psi_{-\mathbf{q}} \rangle_0 = \frac{t}{\epsilon_{\mathbf{q}}} \quad (10.2.18)$$

is the harmonic classical propagator of the non-interacting system. By means of Eqs. (10.2.8) and (10.2.7), one obtains

$$\begin{aligned} \langle \psi_{\mathbf{q}} \psi_{-\mathbf{q}} \mathcal{H}_4 \rangle_0^c &= -\mu^2 S^2 \langle \psi_{\mathbf{q}} \psi_{-\mathbf{q}} \rangle_0^2 \frac{1}{N} \sum_{\mathbf{k}} [D^{xx}(\mathbf{Q}) \\ &\quad + D^{xx}(\mathbf{Q} + \mathbf{q} - \mathbf{k}) - D^{yy}(\mathbf{Q} - \mathbf{q}) - D^{yy}(\mathbf{Q} - \mathbf{k})] \langle \psi_{\mathbf{k}} \psi_{-\mathbf{k}} \rangle_0 \end{aligned} \quad (10.2.19)$$

and

$$\begin{aligned} \langle \psi_{\mathbf{q}} \psi_{-\mathbf{q}} \mathcal{H}_3^2 \rangle_0^c &= \mu^4 S^4 \langle \psi_{\mathbf{q}} \psi_{-\mathbf{q}} \rangle_0^2 \frac{1}{N} \sum_{\mathbf{k}} [D^{xy}(\mathbf{Q} - \mathbf{q})^2 + 4D^{xy}(\mathbf{Q} - \mathbf{q})D^{xy}(\mathbf{Q} - \mathbf{k}) \\ &\quad + 2D^{xy}(\mathbf{Q} - \mathbf{k})^2 + 2D^{xy}(\mathbf{Q} - \mathbf{k})D^{xy}(\mathbf{Q} - \mathbf{k} + \mathbf{q})] \\ &\quad \times \langle \psi_{\mathbf{k}} \psi_{-\mathbf{k}} \rangle_0 \langle \psi_{\mathbf{k}-\mathbf{q}} \psi_{-\mathbf{k}+\mathbf{q}} \rangle_0. \end{aligned} \quad (10.2.20)$$

Then the renormalized classical propagator of the interacting system reads

$$\langle \psi_{\mathbf{q}} \psi_{-\mathbf{q}} \rangle = \frac{1}{\langle \psi_{\mathbf{q}} \psi_{-\mathbf{q}} \rangle_0^{-1} - \Sigma_{\mathbf{q}}} = \frac{t}{\epsilon_{\mathbf{q}} - t \Sigma_{\mathbf{q}}}, \quad (10.2.21)$$

where the proper self-energy  $\Sigma_{\mathbf{q}}$ , obtained from Eqs. (10.2.19) and (10.2.20), is given by

$$\begin{aligned} \Sigma_{\mathbf{q}} &= \frac{1}{N} \sum_{\mathbf{k}} [D^{xx}(\mathbf{Q}) + D^{xx}(\mathbf{Q} + \mathbf{q} - \mathbf{k}) - D^{yy}(\mathbf{Q} - \mathbf{q}) - D^{yy}(\mathbf{Q} - \mathbf{k})] \frac{a^3}{\epsilon_{\mathbf{k}}} \\ &\quad + \frac{1}{2N} \sum_{\mathbf{k}} [D^{xy}(\mathbf{Q} - \mathbf{q})^2 + 4D^{xy}(\mathbf{Q} - \mathbf{q})D^{xy}(\mathbf{Q} - \mathbf{k}) + 2D^{xy}(\mathbf{Q} - \mathbf{k})^2 \\ &\quad + 2D^{xy}(\mathbf{Q} - \mathbf{k})D^{xy}(\mathbf{Q} - \mathbf{k} + \mathbf{q})] \frac{a^6}{\epsilon_{\mathbf{k}} \epsilon_{\mathbf{k}-\mathbf{q}}}. \end{aligned} \quad (10.2.22)$$

The renormalized spectrum is then

$$\hbar\omega(\mathbf{q}) = \frac{\mu^2 S^2}{2a^3} (\epsilon_{\mathbf{q}} - t \Sigma_{\mathbf{q}}). \quad (10.2.23)$$

The self-energy (10.2.22) evaluated at  $\mathbf{q} = \mathbf{q}_0$  gives

$$\begin{aligned} \Sigma_{\mathbf{q}_0} &= \frac{1}{N} \sum_{\mathbf{k}} [D^{xx}(\mathbf{Q} + \mathbf{q}_0 - \mathbf{k}) - D^{yy}(\mathbf{Q} - \mathbf{k})] \frac{a^3}{\epsilon_{\mathbf{k}}} \\ &\quad + \frac{1}{N} \sum_{\mathbf{k}} D^{xy}(\mathbf{Q} - \mathbf{k}) [D^{xy}(\mathbf{Q} - \mathbf{k}) + D^{xy}(\mathbf{Q} - \mathbf{k} + \mathbf{q}_0)] \frac{a^6}{\epsilon_{\mathbf{k}} \epsilon_{\mathbf{k}-\mathbf{q}_0}} \\ &= -0.575 \end{aligned} \quad (10.2.24)$$

so that

$$\hbar\omega(\mathbf{q}_0) = \frac{\mu^2 S^2}{2a^3} 0.575 t. \quad (10.2.25)$$

The gap at  $\mathbf{q} = \mathbf{q}_0$  originates from thermal fluctuations and increases as temperature increases. This behaviour<sup>100</sup> is very peculiar since, usually, the energy gap is *reduced*



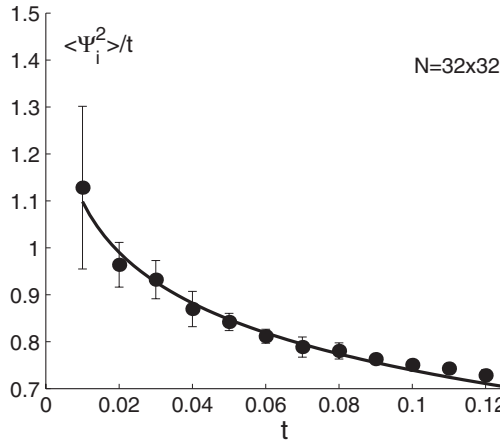


Fig. 10.1. Mean-square angular displacement versus temperature. The continuous curve is the analytic result (10.2.27) with  $O(t) = 0.38t$ . Full circles are MC data for a  $32 \times 32$  SQ lattice.<sup>100</sup>

rather than *increased* by thermal fluctuations. A calculation of the renormalized spectrum in the neighbourhood of  $\mathbf{q}_0$  gives

$$\hbar\omega(\mathbf{q} \rightarrow \mathbf{q}_0) = \frac{\mu^2 S^2}{2a^3} [0.575 t + 0.14474(\pi - aq_x)^2 + 1.7873(\pi - aq_y)^2] \quad (10.2.26)$$

and the mean-square angular displacement (10.2.4), making use of Eq. (10.2.23), becomes

$$\langle \psi_i^2 \rangle = \frac{1}{N} \sum_{\mathbf{k}} \frac{t}{\epsilon_{\mathbf{k}} - t \Sigma_{\mathbf{k}}} \simeq -0.156 t \ln t + O(t), \quad (10.2.27)$$

where the last equality points out the singular contribution to the sum coming from the renormalized spectrum about  $\mathbf{q} = \mathbf{q}_0$ . As one can see from Eq. (10.2.27), at low temperature,  $\langle \psi_i^2 \rangle / t$  diverges logarithmically as shown by the continuous curve in Fig. 10.1, assuming  $O(t) = 0.38t$ . Note that the same quantity evaluated in systems with conventional LRO is a constant since in this case, only the regular contribution  $O(t)$  in the sum (10.2.27) is present. Using the renormalized spectrum, the order parameter (10.2.4) becomes

$$\langle \cos \psi_i \rangle = \cos(l_2 \pi) e^{0.0882 t \ln t}. \quad (10.2.28)$$

Note the infinite slope of the order parameter for  $t \rightarrow 0$ . In this limit, the energy cost to create a spin wave of wavevector  $\mathbf{q} \sim \mathbf{q}_0$  is vanishing so that a large number of spin waves can be excited. However, the interaction between the spin waves creates a gap in the spectrum that increases at increasing temperature and the LRO is restored.

For comparison, we consider the isotropic long range planar antiferromagnet in which the spin-spin coupling decays as  $\frac{1}{r^3}$  where  $r$  is the spin-spin distance. The

Hamiltonian of such a model reads

$$\mathcal{H} = \frac{1}{2} \sum_i \sum_{\mathbf{r} \neq 0} J(r) \mathbf{S}_i \cdot \mathbf{S}_{i+\mathbf{r}} = \frac{1}{2} J a^3 S^2 \sum_i \sum_{\mathbf{r} \neq 0} \frac{1}{r^3} \cos(\mathbf{Q} \cdot \mathbf{r} + \psi_i - \psi_{i+\mathbf{r}}). \quad (10.2.29)$$

The expansion of the Hamiltonian (10.2.29) for small angular displacements gives

$$\mathcal{H} = E_0 + \mathcal{H}_2 + \mathcal{H}_4 + \dots \quad (10.2.30)$$

where

$$E_0 = \frac{1}{2} N S^2 J(\mathbf{Q}), \quad (10.2.31)$$

$$\mathcal{H}_2 = \frac{1}{2} S^2 \sum_{\mathbf{q}} [J(\mathbf{Q} - \mathbf{q}) - J(\mathbf{Q})] \psi_{\mathbf{q}} \psi_{-\mathbf{q}}, \quad (10.2.32)$$

$$\begin{aligned} \mathcal{H}_4 = \frac{1}{24} S^2 \frac{1}{N} \sum_{\mathbf{q}_1, \mathbf{q}_2, \mathbf{q}_3, \mathbf{q}_4} \delta_{\mathbf{q}_1 + \mathbf{q}_2 + \mathbf{q}_3 + \mathbf{q}_4, 0} [J(\mathbf{Q}) - 2J(\mathbf{Q} + \mathbf{q}_4) \\ + 3J(\mathbf{Q} + \mathbf{q}_3 + \mathbf{q}_4) - 2J(\mathbf{Q} - \mathbf{q}_1)] \psi_{\mathbf{q}_1} \psi_{\mathbf{q}_2} \psi_{\mathbf{q}_3} \psi_{\mathbf{q}_4} \end{aligned} \quad (10.2.33)$$

with

$$J(\mathbf{q}) = J a^3 \sum_{\mathbf{r} \neq 0} \frac{1}{r^3} e^{i\mathbf{q} \cdot \mathbf{r}}. \quad (10.2.34)$$

The minimum of  $E_0(\mathbf{Q})$  in Eq. (10.2.31) is obtained for  $\mathbf{Q} = \frac{2\pi}{a}(\frac{1}{2}, \frac{1}{2})$  corresponding to a Néel antiferromagnetic configuration. Note the absence of cubic terms in the angular displacements in the Hamiltonian (10.2.30). The harmonic spin wave approximation gives an elementary excitation energy

$$\hbar\omega_2(\mathbf{q}) = \frac{1}{2} J S^2 \epsilon_{\mathbf{q}} \quad (10.2.35)$$

where

$$\epsilon_{\mathbf{q}} = \frac{1}{J} [J(\mathbf{Q} - \mathbf{q}) - J(\mathbf{Q})] \quad (10.2.36)$$

that vanishes quadratically as  $q \rightarrow 0$ . Indeed, expanding Eq. (10.2.36) about  $\mathbf{q} = 0$ , one obtains

$$\epsilon_{\mathbf{q} \rightarrow 0} = 0.40388 (aq)^2. \quad (10.2.37)$$

The first-order renormalized spin wave spectrum is given by

$$\hbar\omega(\mathbf{q}) = \frac{1}{2} J S^2 (\epsilon_{\mathbf{q}} - t \Sigma_{\mathbf{q}}) \quad (10.2.38)$$

where  $t = \frac{k_B T}{J S^2}$  and

$$\begin{aligned} \Sigma_{\mathbf{q}} = -\frac{1}{JN} \sum_{\mathbf{k}} \left\{ J(\mathbf{Q}) - J(\mathbf{Q} - \mathbf{k}) - J(\mathbf{Q} - \mathbf{q}) \right. \\ \left. + \frac{1}{2} [J(\mathbf{Q} - \mathbf{q} - \mathbf{k}) + J(\mathbf{Q} + \mathbf{q} - \mathbf{k})] \right\} \frac{1}{\epsilon_{\mathbf{k}}} \end{aligned} \quad (10.2.39)$$

that for  $q \rightarrow 0$  vanishes as  $\Sigma_{q \rightarrow 0} = 0.101(aq)^2$ . In the long wavelength limit, both the harmonic and the renormalized spectra vanish quadratically as  $q \rightarrow 0$ , leading to a divergence of the mean-square angular displacement

$$\langle \psi_i^2 \rangle \simeq \langle \psi_i^2 \rangle_0 = \frac{1}{N} \sum_q \frac{t}{\epsilon_q} \simeq -0.39406 \, t \lim_{q \rightarrow 0} \left[ \ln \left( \frac{aq}{2\pi} \right) \right] \rightarrow +\infty \quad (10.2.40)$$

and therefore to the absence of LRO at any finite temperature. For a finite system, one may replace the argument of the logarithmic function in Eq. (10.2.40) by  $\frac{1}{\sqrt{N}}$  where  $N$  is the total number of the spins obtaining

$$\langle \psi_i^2 \rangle_N \simeq 0.19703 \, t \ln N + O(t) \quad (10.2.41)$$

where  $O(t)$  is the regular term independent of  $N$ . Equation (10.2.41) shows that the mean-square angular displacement diverges logarithmically in the thermodynamic limit as shown by the upper continuous curve of Fig. 10.2 for  $t = 0.1$ . The divergence for  $N \rightarrow \infty$  is related to the soft mode at  $\mathbf{q} = 0$  that is not destroyed by thermal fluctuations in the isotropic long range antiferromagnetic planar rotator. This fact could be expected since the rotational invariance of Hamiltonian (10.2.29) implies the existence of a soft mode at  $\mathbf{q} = 0$ .

In order to check the analytic calculation at low temperature and to extend the study of the model at higher temperature, one can perform MC simulations. In particular, the temperature dependence of the mean-square angular displacement can be evaluated and compared with the analytic result at low temperature.<sup>100</sup> As shown in Fig. 10.1, MC data (full circles) fit very well the analytic result (10.2.27) obtained by the renormalized spin wave theory (continuous curve). MC data<sup>100</sup> are taken from a simulation on a sample  $32 \times 32$  averaging over  $10^3$  configurations after having disregarded  $10^5$  steps for equilibration. An approach of periodic “images” is

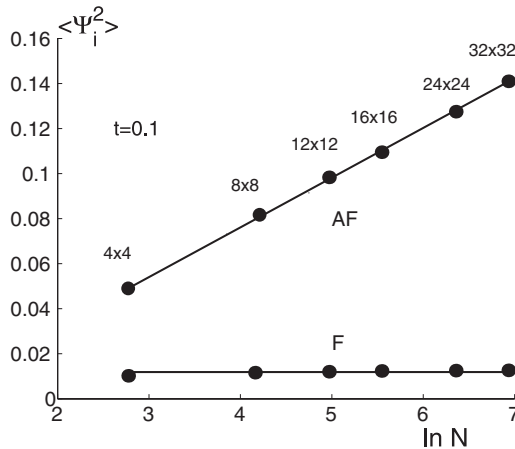


Fig. 10.2. Mean-square angular displacement at  $t = 0.1$  versus  $\ln N$  for SQ planar model with ferromagnetic (F) and antiferromagnetic (AF) isotropic long range interactions decaying as  $\frac{1}{r^3}$ . The full circles are obtained from MC simulations.<sup>100</sup> The continuous curves are the analytic results.

used.<sup>101</sup> Such an approach, which is based on a periodic arrangement of MC cells, seems to be the most convenient method to treat systems with long range interactions. Note that the singular behaviour of the mean-square angular displacement is captured by MC simulation only if the region of low temperature ( $0.01 < t < 0.1$ ) is carefully investigated.

In Fig. 10.2, the size dependence of the mean-square angular displacement at  $t = 0.1$  is shown for the ferromagnetic and antiferromagnetic SQ planar model with isotropic long range interaction decaying as  $1/r^3$  (full circles). The existence of LRO in the ferromagnetic model is supported by the size independence of the mean-square angular displacement (lower curve). On the contrary, the absence of LRO in the antiferromagnetic model is clearly pointed out by the size dependence of the mean-square angular displacement which agrees very well with the analytic result (10.2.41). The existence of LRO in the isotropic long range ferromagnetic planar rotator model can be justified analytically by evaluating the mean-square angular displacement by using the harmonic spin wave approximation. In this case, the ground state corresponds to a ferromagnetic configuration with  $\mathbf{Q} = 0$  and the harmonic spin wave spectrum is given by Eq. (10.2.35) with

$$\epsilon_{\mathbf{q}} = \frac{1}{J}[J(0) - J(\mathbf{q})]. \quad (10.2.42)$$

Expanding Eq. (10.2.42) about  $\mathbf{q} \rightarrow 0$ , one obtains

$$\epsilon_{\mathbf{q} \rightarrow 0} = 2\pi(aq) - 0.97507 (aq)^2. \quad (10.2.43)$$

The linear increment of the harmonic spectrum as a function of the wavevector  $q$  in the ferromagnetic model prevents any divergence of the mean-square angular displacement. Indeed, one obtains

$$\langle \psi_i^2 \rangle_0 = \frac{1}{N} \sum_{\mathbf{q}} \frac{t}{\epsilon_{\mathbf{q}}} = 0.1275 t \quad (10.2.44)$$

and the LRO is recovered. In Fig. 10.2, the lower continuous curve is the analytic result (10.2.44) for  $t = 0.1$ . The agreement between the MC simulation and the harmonic spin wave theory is very good.

### 10.3. Stripes and Checkerboards in 2D Ising Model

The  $S = \frac{1}{2}$ , SQ Ising model with ferromagnetic NN exchange interaction ( $J > 0$ ) and dipole-dipole ( $g$ ) interaction has been extensively investigated<sup>102–107</sup> because of its theoretical interest in studying the effect of long range interactions in the critical region and in view of its possible application in describing the qualitative features of the spin configurations observed in ultrathin films of magnetic atoms on metal substrates. The Hamiltonian of the model is

$$\mathcal{H} = -J \sum_{\langle i,j \rangle} \sigma_i \sigma_j + g \sum_{i \neq j} \frac{1}{r_{ij}^3} \sigma_i \sigma_j, \quad (10.3.1)$$

where the first sum is restricted to distinct pairs of NN spins and a ferromagnetic interaction  $J > 0$  is assumed; in the second sum,  $i$  and  $j$  run over all the

sites of a SQ lattice with  $L \times L = N$  and  $g = \frac{\mu_B S^2}{a^3}$ . The spins  $\sigma_i = \pm 1$  are supposed to be aligned out-of-plane. The analytic investigation of the zero temperature energy of Eq. (10.3.1) leads to a variety of configurations depending on the ratio  $J/g$ . The *stripe* and *checkerboard* configurations can be obtained assuming a double periodic spin configuration of the ground state. In particular, let us assume a periodic spin configuration with period  $p_1 = 2h_1$  along the  $x$ -axis and  $p_2 = 2h_2$  along the  $y$ -axis of a SQ lattice of size  $L$  where  $L$  is an even number and label each lattice site by a couple of integer numbers  $(n, m)$  with  $n, m = 1, \dots, L$ . The double periodicity implies that the spin  $\sigma_{m,n}$  at site  $\mathbf{r}_i = (m, n)$  is the same as the spin  $\sigma_{m+s_1 p_1, n+s_2 p_2}$  at site  $(m+s_1 p_1, n+s_2 p_2)$  with  $s_1 = 0, 1, \dots, L/p_1 - 1$  and  $s_2 = 0, 1, \dots, L/p_2 - 1$ . The *finite* Fourier transform of the spin  $\sigma_{m,n}$  is given by

$$\begin{aligned}\sigma_{\mathbf{Q}} \equiv \sigma_{q_1, q_2} &= \frac{1}{L} \sum_{m=1}^L \sum_{n=1}^L \sigma_{m,n} e^{-i \frac{2\pi}{L} q_1 m} e^{-i \frac{2\pi}{L} q_2 n} \\ &= \frac{1}{L} \sum_{m=1}^{p_1} \sum_{n=1}^{p_2} \sigma_{m,n} e^{-i \frac{2\pi}{L} q_1 m} e^{-i \frac{2\pi}{L} q_2 n} \sum_{s_1=0}^{L/p_1-1} \sum_{s_2=1}^{L/p_2-1} e^{-i \frac{2\pi}{L} q_1 s_1 p_1} e^{-i \frac{2\pi}{L} q_2 s_2 p_2}\end{aligned}\quad (10.3.2)$$

where  $\mathbf{Q} = 2\pi(\frac{q_1}{L}, \frac{q_2}{L})$  with  $q_1, q_2 = 0, 1, \dots, L-1$ . The last two sums occurring in Eq. (10.3.2) can be easily performed. Indeed,

$$\sum_{s_1=0}^{L/p_1-1} e^{-i \frac{2\pi}{L} q_1 s_1 p_1} = \frac{L}{p_1} \delta_{\frac{q_1}{L}, \frac{l_1}{p_1}}, \quad (10.3.3)$$

where  $l_1 = 0, 1, \dots, p_1 - 1$ . Then Eq. (10.3.2) reduces to

$$\sigma_{q_1, q_2} = \frac{L}{p_1 p_2} \delta_{\frac{q_1}{L}, \frac{l_1}{p_1}} \delta_{\frac{q_2}{L}, \frac{l_2}{p_2}} \sum_{m=1}^{p_1} \sum_{n=1}^{p_2} \sigma_{m,n} e^{-i \frac{2\pi}{L} q_1 m} e^{-i \frac{2\pi}{L} q_2 n}. \quad (10.3.4)$$

To perform the sums occurring in Eq. (10.3.4), one has to account for the checkerboard structure of the ground state. Indeed, one takes  $\sigma_{m,n} = 1$  for  $1 \leq m \leq h_1$ ,  $1 \leq n \leq h_2$  and  $h_1 + 1 \leq m \leq 2h_1$ ,  $h_2 + 1 \leq n \leq 2h_2$  and  $\sigma_{m,n} = -1$  for  $1 \leq m \leq h_1$ ,  $h_2 + 1 \leq n \leq 2h_2$  and  $h_1 + 1 \leq m \leq 2h_1$ ,  $1 \leq n \leq h_2$ . Then the sums in Eq. (10.3.4) become

$$\begin{aligned}\sum_{m=1}^{p_1} \sum_{n=1}^{p_2} \sigma_{m,n} e^{-i \frac{2\pi}{L} q_1 m} e^{-i \frac{2\pi}{L} q_2 n} &= \sum_{m=1}^{h_1} \sum_{n=1}^{h_2} e^{-i \frac{2\pi}{L} q_1 m} e^{-i \frac{2\pi}{L} q_2 n} \\ &\quad \times (1 - e^{-i \frac{2\pi}{L} q_1 h_1}) (1 - e^{-i \frac{2\pi}{L} q_2 h_2}).\end{aligned}\quad (10.3.5)$$

Accounting for the  $\delta$ -functions occurring in Eq. (10.3.4), from Eq. (10.3.5) one obtains the relationship

$$\delta_{\frac{q_1}{L}, \frac{l_1}{p_1}} (1 - e^{-i\frac{2\pi}{L}q_1 h_1}) \sum_{m=1}^{h_1} e^{-i\frac{2\pi}{L}q_1 m} = \begin{cases} 0 & \text{for } \frac{q_1}{L} = \frac{s_1}{h_1}, \\ \frac{4e^{-i\frac{\pi}{h_1}(2s_1+1)}}{1 - e^{-i\frac{\pi}{h_1}(2s_1+1)}} & \text{for } \frac{q_1}{L} = \frac{s_1 + \frac{1}{2}}{h_1} \end{cases} \quad (10.3.6)$$

with  $s_1 = 0, 1, \dots, h_1 - 1$ . Replacing the result (10.3.6) into Eq. (10.3.4), one has

$$\sigma_{q_1, q_2} = \frac{4L}{h_1 h_2} \delta_{\frac{q_1}{L}, \frac{l_1}{h_1}(s_1 + \frac{1}{2})} \delta_{\frac{q_2}{L}, \frac{l_2}{h_2}(s_2 + \frac{1}{2})} \frac{e^{-i\frac{\pi}{h_1}(2s_1+1)}}{1 - e^{-i\frac{\pi}{h_1}(2s_1+1)}} \times \frac{e^{-i\frac{\pi}{h_2}(2s_2+1)}}{1 - e^{-i\frac{\pi}{h_2}(2s_2+1)}} \quad (10.3.7)$$

with  $s_1 = 0, 1, \dots, h_1 - 1$  and  $s_2 = 0, 1, \dots, h_2 - 1$ . The square modulus of Eq. (10.3.7) is given by

$$|\sigma_{q_1, q_2}|^2 = \frac{L^2}{h_1^2 h_2^2} \delta_{\frac{q_1}{L}, \frac{l_1}{h_1}(s_1 + \frac{1}{2})} \delta_{\frac{q_2}{L}, \frac{l_2}{h_2}(s_2 + \frac{1}{2})} \frac{1}{\sin^2 \left[ \frac{\pi}{h_1} \left( s_1 + \frac{1}{2} \right) \right] \sin^2 \left[ \frac{\pi}{h_2} \left( s_2 + \frac{1}{2} \right) \right]} \quad (10.3.8)$$

and the general formula for the ground-state energy of a checkerboard configuration with ferromagnetic NN exchange and dipole-dipole interaction becomes

$$\begin{aligned} E_{\langle h_1, h_2 \rangle} &= - \sum_{q_1, q_2} \left[ J \left( \cos \frac{2\pi q_1}{L} + \cos \frac{2\pi q_2}{L} \right) + g D^{zz} \left( \frac{q_1}{L}, \frac{q_2}{L} \right) \right] |\sigma_{q_1, q_2}|^2 \\ &= - \frac{L^2}{h_1^2 h_2^2} \sum_{s_1=0}^{h_1-1} \sum_{s_2=0}^{h_2-1} \left\{ J \left[ \cos \frac{2\pi(s_1 + \frac{1}{2})}{h_1} + \cos \frac{2\pi(s_2 + \frac{1}{2})}{h_2} \right] \right. \\ &\quad \left. + g D^{zz} \left( \frac{s_1 + \frac{1}{2}}{h_1}, \frac{s_2 + \frac{1}{2}}{h_2} \right) \right\} \frac{1}{\sin^2 \left[ \frac{\pi}{h_1} \left( s_1 + \frac{1}{2} \right) \right] \sin^2 \left[ \frac{\pi}{h_2} \left( s_2 + \frac{1}{2} \right) \right]}, \end{aligned} \quad (10.3.9)$$

where  $D^{zz}(\mathbf{Q}) \equiv D^{zz}(\frac{q_1}{L}, \frac{q_2}{L})$  is given by Eq. (10.1.21). From the relationships

$$\frac{1}{h^2} \sum_{s=0}^{h-1} \frac{1}{\sin^2 \left[ \frac{\pi}{h} \left( s + \frac{1}{2} \right) \right]} = 1 \quad (10.3.10)$$

and

$$\frac{1}{h^2} \sum_{s=0}^{h-1} \frac{\cos \left[ \frac{2\pi}{h} \left( s + \frac{1}{2} \right) \right]}{\sin^2 \left[ \frac{\pi}{h} \left( s + \frac{1}{2} \right) \right]} = 1 - \frac{2}{h}, \quad (10.3.11)$$

one obtains

$$\begin{aligned} \frac{E_{\langle h_1, h_2 \rangle}}{gL^2} &= -2 \frac{J}{g} \left( 1 - \frac{1}{h_1} - \frac{1}{h_2} \right) \\ &\quad - \frac{1}{h_1^2 h_2^2} \sum_{s_1=0}^{h_1-1} \sum_{s_2=0}^{h_2-1} \frac{D^{zz} \left( \frac{s_1 + \frac{1}{2}}{h_1}, \frac{s_2 + \frac{1}{2}}{h_2} \right)}{\sin^2 \left[ \frac{\pi}{h_1} \left( s_1 + \frac{1}{2} \right) \right] \sin^2 \left[ \frac{\pi}{h_2} \left( s_2 + \frac{1}{2} \right) \right]}. \end{aligned} \quad (10.3.12)$$

Equation (10.3.12) is the general zero temperature energy of a *checkerboard* configuration where blocks of  $h_1 \times h_2$  spins up and down alternate in the SQ lattice. A study has to be done to determine the regions of stability of the different checkerboard configurations as function of the ratio  $J/g$ . The checkerboard configuration was proposed as possible ground-state configuration of an Ising model with NN exchange and dipolar interactions by Czech and Villain<sup>108</sup> in the limit of large  $J/g$ . They arrived at the conclusion that for  $\langle h_1, h_2 \rangle$  configurations with  $h_1, h_2 \rightarrow \infty$ , the ground-state energy was characterized by a *regular* checkerboard configuration with  $h_1 = h_2$ . On the other hand, *stripe* configurations corresponding to  $\langle h_1, h_2 \rightarrow \infty \rangle$  or  $\langle h_1 \rightarrow \infty, h_2 \rangle$  were proven to have a lower energy with respect to the checkerboard configurations,<sup>109</sup> at least for small  $J/g$ . A careful investigation of the minima of the function (10.3.12) varying the ratio  $J/g$  shows<sup>107</sup> that the checkerboard configuration is never stable for generic  $\langle h_1, h_2 \rangle$ . Only the checkerboard phases corresponding to  $h_1 = 1$  and  $h_2 \equiv n = 1, 2, \dots$  become stable in a restricted region of  $J/g$ . For the checkerboard phase  $\langle 1, n \rangle$ , the zero temperature energy (10.3.12) becomes

$$\frac{E_{\langle 1, n \rangle}}{gL^2} = \frac{2}{n} \left( \frac{J}{g} \right) - \frac{1}{n^2} \sum_{s=0}^{n-1} \frac{D^{zz} \left( \frac{1}{2}, \frac{1}{n} \left( s + \frac{1}{2} \right) \right)}{\sin^2 \left[ \frac{\pi}{n} \left( s + \frac{1}{2} \right) \right]} \equiv a \frac{J}{g} + b. \tag{10.3.13}$$

In Table 10.2, we give the coefficients  $a$  and  $b$  and the region of stability for several  $\langle 1, n \rangle$  phases obtained from Eq. (10.3.13). For instance, the Néel antiferromagnet, corresponding to the checkerboard configuration  $\langle 1, 1 \rangle$  ( $n = 1$  in Table 10.2), is stable for  $J/g < 0.83040611$  in agreement with the result (10.1.22) obtained for the Ising model with pure dipole–dipole interaction. In the narrow range  $0.83040611750 < J/g < 0.880624471981$ , the sequence of  $\langle 1, n \rangle$ -phases, with  $n = 2, 3, \dots, 9$ , appears. Each phase is characterized by  $n$  identical antiferromagnetic rows followed by the same number of antiferromagnetic rows with overturned spins. For  $n \geq 10$ , all the checkerboard phases collapse to the multiphase point  $J/g = 0.880624471981$ . Note that for  $n \rightarrow \infty$ , the checkerboard phase reduces to a stripe configuration corresponding to a “columnar” phase in which ferromagnetic

Table 10.2. Coefficients  $a$  and  $b$  of the zero temperature energy  $E_{\langle 1, n \rangle} / (gL^2) = a(J/g) + b$  for several  $\langle 1, n \rangle$  phases.

$n$	$a$	$b$	Region of stability
1	2	−2.6458865323	(0, 0.830406111750)
2	1	−1.8154804206	(0.830406111750, 0.878839805732)
3	2/3	−1.5225338186	(0.878839805732, 0.880558140666)
4	1/2	−1.3757741285	(0.880558140666, 0.880621920068)
5	2/5	−1.2877119365	(0.880621920068, 0.880624371628)
6	1/3	−1.2290036451	(0.880624371628, 0.880624467975)
7	2/7	−1.1870691466	(0.880624467975, 0.880624471820)
8	1/4	−1.1556182726	(0.880624471820, 0.880624471975)
9	2/9	−1.1311564817	(0.880624471975, 0.880624471981)
$n \geq 10$	$2/n$	$−0.9354621546 − \frac{1.761248944}{n}$	$\frac{J}{g} = 0.880624471981$

columns of spin up and down alternate. As shown in Table 10.2, the width  $n$  of the bands that are made up of repeated antiferromagnetic rows becomes larger and larger as  $J/g$  increases. For  $n \geq 10$ , one can see that the coefficient  $b$  occurring in Eq. (10.3.13) is given by

$$b = D^{zz} \left( \frac{1}{2}, 0 \right) + \frac{1.761248944}{n} \quad (10.3.14)$$

where  $D^{zz}(\frac{1}{2}, 0)$  is given in Table 10.1. Then for  $n \geq 10$ , the checkerboard energy (10.3.13) becomes

$$\frac{E_{\langle 1, n \rangle}}{gL^2} = \frac{2}{n} \left( \frac{J}{g} \right) - 0.9354621546 - \frac{1.761248944}{n}. \quad (10.3.15)$$

Note that for  $J/g = 0.8808624471981$ , the energy of the  $\langle 1, n \rangle$  phase is independent of  $n$  and an “accumulation point” occurs, similar to the *multiphase point* ( $T = 0, J_2/J_1 = -1/2$ ) present in the anisotropic next nearest neighbour Ising (ANNNI) model<sup>110</sup> in 2D and 3D where the competition between the NN interaction  $J_1$  and the NNN interaction  $J_2$  is restricted to one direction (i.e. the  $x$ -axis) of a SQ or SC lattice. In Fig. 10.3, we show the checkerboard configurations  $\langle 1, 1 \rangle$ ,  $\langle 1, 2 \rangle$ ,  $\langle 1, 3 \rangle$  and the stripe configuration  $\langle 1, \infty \rangle$  for a SQ lattice of

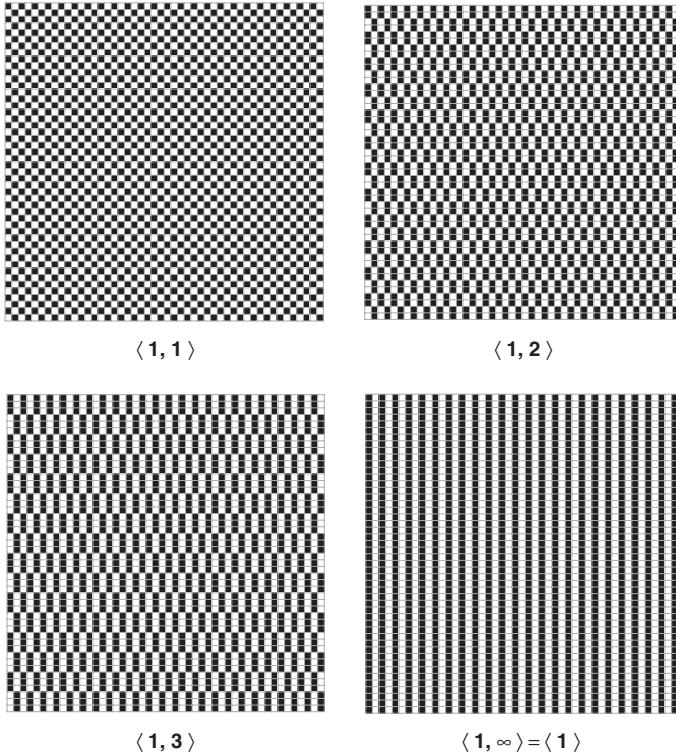


Fig. 10.3. Zero temperature configuration of the phases  $\langle 1, 1 \rangle$  (upper left),  $\langle 1, 2 \rangle$  (upper right),  $\langle 1, 3 \rangle$  (lower left) and  $\langle 1, \infty \rangle$  (lower right).



side  $L = 48$ . The white and black squares correspond to spins of opposite orientation. As one can see, the  $\langle 1, n \rangle$  phases correspond to irregular checkerboard. We stress that the checkerboard phases have energy lower than the stripe phases in a very narrow region of  $J/g$  located between the Néel phase and the columnar phase. Any other checkerboard configuration  $\langle m, n \rangle$  with  $m \neq 1$  is *never* stable for any  $J/g$ .

As we have seen, the *stripe* configuration can be obtained from the checkerboard configuration taking the limit  $h_1 \rightarrow \infty$  (horizontal stripes of width  $h_2$ ) or  $h_2 \rightarrow \infty$  (vertical stripes of width  $h_1$ ). The energies of the stripe configurations are obtained from Eq. (10.3.12), assuming  $h_1 = h$ ,  $h_2 \rightarrow \infty$  or  $h_1 \rightarrow \infty$ ,  $h_2 = h$  and making use of Eq. (10.3.10). The general stripe configuration energy becomes

$$\frac{E_{\langle h \rangle}}{gL^2} = -2\frac{J}{g} \left(1 - \frac{1}{h}\right) - \frac{1}{h^2} \sum_{s=0}^{h-1} \frac{D^{zz}\left(0, \frac{s+\frac{1}{2}}{h}\right)}{\sin^2\left[\frac{\pi}{h}\left(s + \frac{1}{2}\right)\right]}. \tag{10.3.16}$$

The energies of several stripe configurations are given in Table 10.3. The zero temperature energy of the ferromagnetic configuration is obtained taking the limit  $h \rightarrow \infty$  of Eq. (10.3.16), that is,

$$\frac{E_F}{gL^2} = -2\frac{J}{g} - D^{zz}(0, 0) \tag{10.3.17}$$

Table 10.3. Coefficients  $a$  and  $b$  of the zero temperature energy  $E_{\langle h \rangle}/(gL^2) = a(J/g) + b$  for stripe configurations of width  $h$ .

$h$	$a$	$b$	Region of stability
1	0	-0.9354621546	(0.880625, 2.517077)
2	-1	1.5816148819	(2.517077, 4.344909)
3	-4/3	3.0299178788	(4.344909, 5.628990)
4	-3/2	3.9680829288	(5.628990, 6.608484)
5	-8/5	4.6893131395	(6.608484, 7.398049)
6	-5/3	5.1221346075	(7.398049, 8.058698)
7	-12/7	5.5058821312	(8.058698, 8.626345)
8	-7/4	5.8139658640	(8.626345, 9.123814)
9	-16/9	6.0674051477	(9.123814, 9.566483)
10	-9/5	6.2799936626	(9.566483, 9.965190)
11	-20/11	6.4611789296	(9.965190, 10.327855)
12	-11/6	6.6176615768	(10.327855, 10.660440)
13	-24/13	6.7543338863	(10.660440, 10.967544)
14	-13/7	6.8748563518	(10.967544, 11.252788)
15	-28/15	6.9820257605	(11.252788, 11.519072)
16	-15/8	7.0780180265	(11.519072, 11.768757)
17	-32/17	7.1645530020	(11.768757, 12.003788)
18	-17/9	7.2430091326	(12.003788, 12.225789)
19	-36/19	7.3145049739	(12.225789, 12.436127)
20	-19/10	7.3799582736	(12.436127, 12.635966)
$h \geq 20$	$-2(1 - \frac{1}{h})$	$9.0336216831 - \frac{8}{h} \ln h - \frac{9.10467}{h} - \frac{1.09642}{h^3}$	

where  $D^{zz}(0,0)$  is given in Table 10.1. For stripes of large width ( $h \geq 20$ ), Eq. (10.3.16) is well represented by the formula

$$\frac{E_{\langle h \rangle}}{gL^2} = -2\frac{J}{g} \left(1 - \frac{1}{h}\right) - D^{zz}(0,0) - \frac{8}{h} \ln h - \frac{9.10467}{h} - \frac{1.09642}{h^3}. \quad (10.3.18)$$

The energies obtained from Eq. (10.3.18) differ from those obtained by direct (numerical) calculation by less than  $10^{-6}$  for  $20 < h < 10^5$ . The logarithmic term in the asymptotic expansion (10.3.18) is reminiscent of the linear dependence on the magnitude  $Q = |\mathbf{Q}|$  of  $D^{zz}(\mathbf{Q})$  for  $\mathbf{Q} \rightarrow 0$ , that is

$$a^3 D^{zz}(\mathbf{Q}) = -9.0336216831 + 2\pi(aQ) - 0.975066230(aQ)^2 \dots \quad (10.3.19)$$

In Fig. 10.4, we show the stripe configurations  $\langle 2 \rangle$ ,  $\langle 3 \rangle$ ,  $\langle 4 \rangle$  and  $\langle 8 \rangle$  for a SQ lattice of side  $L = 48$ . For  $J/g$  increasing from the multiphase point ( $J/g = 0.880624471981$ ), a sequence of stripe configurations  $\langle h \rangle$  with  $h = 1, 2, \dots$  occurs until the ferromagnetic phase F corresponding to  $h \rightarrow \infty$  is reached. The transition between the F phase and the widest stripe phase  $\langle L/2 \rangle$  occurs at  $J/g = 1.79975 +$

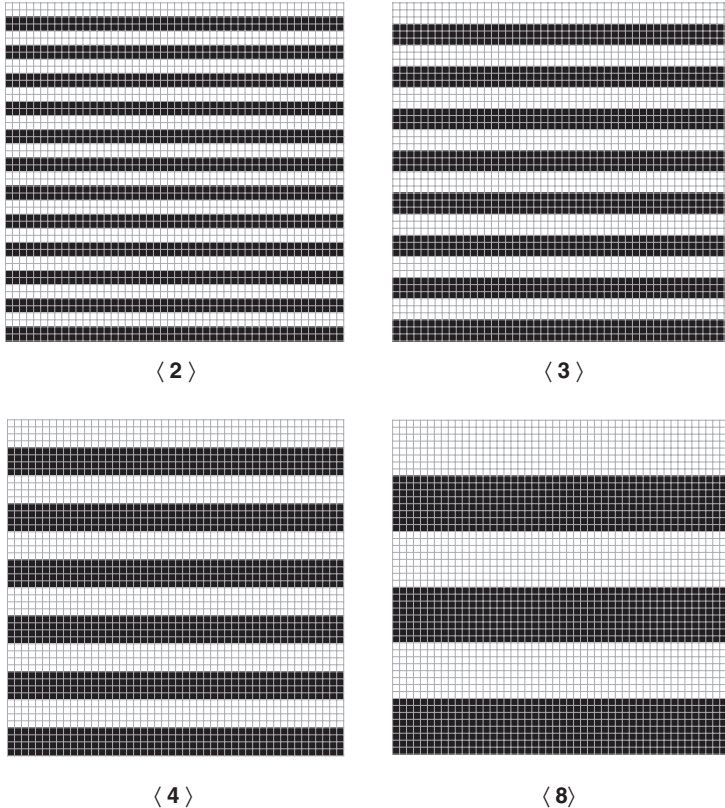


Fig. 10.4. Zero temperature configuration of the stripe phases  $\langle 2 \rangle$  (upper left),  $\langle 3 \rangle$  (upper right),  $\langle 4 \rangle$  (lower left) and  $\langle 8 \rangle$  (lower right).

$\ln L^4$  as it can be obtained by comparing the energy of the F phase with that of the stripe phase with  $h = L/2$  given by the asymptotic expansion (10.3.18).

The structure factor of a checkerboard configuration can be obtained from Eq. (3.1.2). Noticing that the Ising Hamiltonian (10.3.1) commutes with each local spin observable  $\sigma_i$ , one deduces that *all*  $\sigma_i$  are constants of motion, that is  $\sigma_i(t) = \sigma_i$ . This property reduces Eq. (3.1.2) to

$$S^{zz}(\mathbf{Q}, \omega) = \sum_{i,j} e^{i\mathbf{Q} \cdot (\mathbf{r}_i - \mathbf{r}_j)} \langle \sigma_i \sigma_j \rangle \delta(\omega). \quad (10.3.20)$$

Using Eq. (10.3.2), one obtains

$$S^{zz}(\mathbf{Q}, \omega) = N^2 \delta(\omega) \langle S(\mathbf{Q}) \rangle \quad (10.3.21)$$

where  $N = L^2$  and

$$S(\mathbf{Q}) = \frac{|\sigma_{\mathbf{Q}}|^2}{L^2} \quad (10.3.22)$$

is the static structure factor. At zero temperature, the static structure factor for a checkerboard configuration can be obtained directly from Eq. (10.3.8):

$$S(\mathbf{Q}) = \frac{1}{h_1^2 h_2^2 \sin^2\left(\frac{Q_x}{2}\right) \sin^2\left(\frac{Q_y}{2}\right)} \delta_{Q_x, \frac{2\pi}{h_1}(s_1 + \frac{1}{2})} \delta_{Q_y, \frac{2\pi}{h_2}(s_2 + \frac{1}{2})}. \quad (10.3.23)$$

As one can see, the structure factor of a checkerboard configuration consists of a series of  $\delta$ -like elastic peaks located at  $\mathbf{Q} = \left[\frac{2\pi}{h_1}(s_1 + \frac{1}{2}), \frac{2\pi}{h_2}(s_2 + \frac{1}{2})\right]$  with intensities depending on  $\mathbf{Q}$ . Analogously, the following is obtained for a stripe configuration:

$$S(\mathbf{Q}) = \frac{1}{h^2 \sin^2\left[\frac{\pi}{h}(s + \frac{1}{2})\right]} \delta_{Q_x, 0} \delta_{Q_y, \frac{2\pi}{h}(s + \frac{1}{2})}. \quad (10.3.24)$$

#### 10.4. Monte Carlo Simulation

The MC simulation is the most commonly used type of numerical calculation to obtain the thermodynamic properties of a model Hamiltonian at finite temperature. It involves performing long time averages of the physical observables. In particular, for a spin lattice, the thermal average of an observable, say  $\langle \mathcal{O}(\{\sigma_i\}) \rangle$ , is evaluated by taking the value of  $\mathcal{O}$  on a selected number of microscopic states  $\{\sigma_i\}$  among the  $2^N$  states of the whole statistical ensemble: the selection of the microscopic states is performed by reversing a given spin located at the lattice site  $i$  (*single move*) and evaluating the energy of the new configuration  $E_{\text{new}}$ : if the new energy is lower than the energy of the previous configuration  $E_{\text{old}}$ , the move is accepted, and the new configuration is assumed. If the new energy is higher than the old one, then one compares the quantity  $\exp(-\frac{\Delta E}{k_B T}) < 1$  where  $\Delta E = E_{\text{new}} - E_{\text{old}}$  with a random number  $z$  with  $0 < z < 1$ : if  $z < \exp(-\frac{\Delta E}{k_B T})$ , the move is accepted, otherwise the spin reversal is refused. This procedure is called importance-sampling Monte Carlo calculation.<sup>111</sup> A MC *step* (MCS) consists of  $L^2$  spin-flip trials, one for every spin of the lattice. The statistical average  $\langle \mathcal{O} \rangle$  reduces to the arithmetic average of  $\mathcal{O}$

over the selected configurations (*snapshots*). To obtain a reliable statistics, one has to perform long MC *runs* ( $10^5$  MCSs in the present case) recording one configuration every 10 MCSs and disregarding the initial  $10^4$  MCSs for equilibration at each temperature. In order to improve the statistics, an average over eight independent runs was considered.<sup>107</sup> A convenient procedure that allow us to reduce the equilibration time consists of starting from the low temperature configuration (ground state) which is known exactly, increasing the temperature by small steps  $\Delta T = 0.01$  (in units of  $\frac{g}{k_B}$ ) and assuming the starting configuration of the next temperature as the final configuration of the previous one. In this way, the system is always kept near the equilibrium even though near a first-order phase transition, a small uncertainty about the transition temperature between the two coexisting phases is entered because of the reluctance of the system to change its configuration due to the use of single moves. However, the approach based on a gradual rise of the temperature gives accurate results everywhere except in the proximity of a first-order phase transition. Moreover, this approach saves computing time with respect to the approach that assumes a random configuration as initial configuration at any temperature so increasing the equilibration time.<sup>106</sup> Indeed, a serious problem of computing time occurs due to the long range nature of the dipole–dipole interaction: the computing time is proportional to  $L^2$  for a system with short range (exchange) interaction while it grows as  $L^4$  for systems with long range (dipolar) interaction. With the actually available computers the time required for one MCS on a SQ lattice with  $L = 48$  is of the order of  $10^{-2}$  s, so that it is easy to evaluate the time required for a MC simulation. Another problem implicit in the long range interactions is how to cut them on a *finite* lattice: Kretschmer and Binder<sup>101</sup> showed that in MC simulations, the most effective approach is to think of the finite lattice of side  $L$  as a “cell” belonging to an infinite lattice made up of infinitely repeated “images” of the original cell. Then the true dipole–dipole interaction between the spins  $\sigma_i$  and  $\sigma_j$  belonging to the finite lattice under investigation is replaced by an effective interaction that accounts for the interaction of the spin  $\sigma_i$  with *all* the images of the spin  $\sigma_j$  belonging to the infinitely repeated cells. Then we evaluate such an interaction by means of the Ewald’s method of Section 10.1. Obviously, this approach results in an excess of “order” due to the assumption of the periodic image arrangement. Finally, the usual PBC are imposed on the finite lattice.

Among the several thermodynamic quantities that one can evaluate by means of the MC simulation, we will consider the specific heat

$$C = \frac{\langle \mathcal{H}^2 \rangle - \langle \mathcal{H} \rangle^2}{L^2 k_B T^2}, \quad (10.4.1)$$

the internal energy per spin in units of dipolar interaction

$$E = \frac{\langle \mathcal{H} \rangle}{L^2 g}, \quad (10.4.2)$$

the static structure factor  $S(\mathbf{Q})$  given by Eq. (10.3.22) and the order parameter

$$O_{hv} = \left\langle \left| \frac{n_h - n_v}{n_h + n_v} \right| \right\rangle, \quad (10.4.3)$$

where  $n_h$  (respectively,  $n_v$ ) is the number of horizontal (respectively, vertical) pairs of NN antiparallel spins. At  $T = 0$ , this unconventional order parameter is 1 in the stripe configuration since  $n_h = 0$ ,  $n_v = \frac{L}{h}$  for horizontal stripes of width  $h$  and  $n_h = \frac{L}{h}$ ,  $n_v = 0$  for vertical stripes of width  $h$ ; it is  $\frac{n-1}{n+1}$  in the checkerboard phase  $\langle 1, n \rangle$ ; it vanishes in the Néel (N) configuration ( $n_h = n_v = L$ ) and it is indeterminate in the ferromagnetic (F) configuration ( $n_h = n_v = 0$ ). In the last two cases, the order parameter (10.4.3) is replaced by the staggered or sublattice magnetization in the N phase and by the magnetization in the F phase, respectively.

Other quantities that we will investigate in the MC simulation are the energy density distribution  $P(E)$  and the order parameter density distribution  $P(O_{hv})$ . These quantities are particularly useful to establish the order of the phase transition: indeed, a two-peak structure in  $P(E)$  is expected if the phase transition is of the first-order while a single peak that broadens at the transition is expected in a second-order phase transition.<sup>113,114</sup> The two peaks in  $P(E)$  occurring at the first-order phase transition are related to the energies of the two coexisting phases and the transition temperature will be determined as the temperature at which the two peaks have the same area. Indeed, for a finite system, the existence of the two peaks, even though with different areas, is recorded over a narrow but finite range of temperatures at variance with a macroscopic system ( $L \rightarrow \infty$ ) where the coexistence is restricted to a single temperature: the transition temperature of the first-order phase transition. As for the order parameter density distribution<sup>104</sup>  $P(O_{hv})$ , it is more convenient to neglect the absolute value in Eq. (10.4.3): in this way, we are able to distinguish between horizontal ( $O_{hv} = 1$  at  $T = 0$ ) and vertical ( $O_{hv} = -1$  at  $T = 0$ ) stripe phases and a three-peak structure in  $P(O_{hv})$  can be observed at a first-order phase transition: the central peak corresponds to the paramagnetic phase while the two symmetric peaks around the origin correspond to horizontal and vertical stripes respectively. The coexistence of these two peaks is traced back to the occurrence of a “tetragonal” phase<sup>112</sup> where the orientational order is lost because the stripes rotate freely, the paramagnetic phase entering only at higher temperature. The tetragonal phase differs from the conventional paramagnetic phase because it is characterized by a two-peak profile in  $P(O_{hv})$  without the central peak. In both tetragonal and paramagnetic phase, the LRO is absent: it is the short range order that differs in the two phases. Strictly speaking, no phase transition is expected between the tetragonal and paramagnetic phase.

Any MC simulation is performed on a SQ lattice  $48 \times 48$  with PBC.<sup>107</sup> The size of the lattice is suggested by the fact that it is the smallest one supporting stripes of width  $h = 1, 2, 3$  and 4. The remaining stripes consistent with  $L = 48$  are 6, 8, 12 and 24. In Table 10.4, we give the zero temperature energies and the stability regions of the  $\langle 1, n \rangle$  and  $\langle h \rangle$  configurations which are *consistent* with the PBC of the lattice  $48 \times 48$ . Comparing Table 10.4 with Tables 10.2 and 10.3, one can check

Table 10.4. Coefficients  $a$  and  $b$  of the zero temperature energy for  $\langle 1, n \rangle$  and  $\langle h \rangle$  configurations which are consistent with a SQ lattice of side  $L = 48$  and PBC.

$\langle 1, n \rangle, \langle h \rangle$	$a$	$b$	Region of stability
$\langle 1, 1 \rangle = \text{N}$	2	-2.6458865323	(0, 0.830406)
$\langle 1, 2 \rangle$	1	-1.8154804206	(0.830406, 0.878840)
$\langle 1, 3 \rangle$	2/3	-1.5225338186	(0.878840, 0.880558)
$\langle 1, 4 \rangle$	1/2	-1.3757741285	(0.880558, 0.880622)
$\langle 1, 6 \rangle$	1/3	-1.2290036451	(0.880622, 0.880624)
$\langle 1, 8 \rangle$	1/4	-1.1556182726	$\frac{J}{g} = 0.880624$
$\langle 1, \infty \rangle = \langle 1 \rangle$	0	-0.9354621546	(0.880624, 2.517077)
$\langle 2 \rangle$	-1	1.5816148819	(2.517077, 4.344909)
$\langle 3 \rangle$	-4/3	3.0299178788	(4.344909, 5.628990)
$\langle 4 \rangle$	-3/2	3.9680829288	(5.628990, 6.924310)
$\langle 6 \rangle$	-5/3	5.1221346075	(6.924310, 8.301975)
$\langle 8 \rangle$	-7/4	5.8139658640	(8.301975, 9.644349)
$\langle 12 \rangle$	-11/6	6.6176615768	(9.644349, 11.726019)
$\langle 24 \rangle$	-23/12	7.5948298428	(11.726019, 17.265502)
$\langle \infty \rangle = \text{F}$	-2	9.0336216831	$\frac{J}{g} > 17.265502$

the merits and the faults of the finite-size lattice. In the finite-size lattice, some checkerboard and stripe phases disappear from the sequence of the infinite lattice. Indeed, checkerboard  $\langle 1, n \rangle$  and stripe  $\langle h \rangle$  phases with  $n$  and  $h$  such that  $L/(2n)$  and  $L/(2h)$  are *not* integer numbers are prevented by the PBC. By construction, the periodic images assumption implies that the checkerboard and stripe configurations that are consistent with the finite lattice, have the same zero temperature energy  $E$  of the corresponding configurations of the infinite lattice. The lattice  $48 \times 48$ , however, prevents the occurrence of phases with  $n$  and  $h = 5, 7, 9, 10$ , etc. Indeed, the existence regions of the “regular” stripe phases  $\langle 4 \rangle$ ,  $\langle 6 \rangle$  and  $\langle 8 \rangle$  become wider at the expense of the stripe phases  $\langle 5 \rangle$  and  $\langle 7 \rangle$ . However, some “irregular” stripe phases reminiscent of the regular stripe phases suppressed by the finite-size effect reappear.<sup>107</sup> Indeed, a configuration consisting of two stripes of width  $h = 4$  followed by eight stripes of width  $h = 5$  ( $\langle 4^2 5^8 \rangle$ ) becomes stable in the range  $6.63 < J/g < 7.23$  in the lattice  $48 \times 48$ , while it is *never* stable in the infinite lattice where the phase  $\langle 5 \rangle$  has a lower energy. Let us define the phase  $\langle 4^2 5^8 \rangle$  as  $\langle \sim 5 \rangle$  because of its vague recollection to the stripe phase  $\langle 5 \rangle$  of the infinite lattice. An analogous phase  $\langle \sim 7 \rangle$  should be expected between the stripe phases  $\langle 6 \rangle$  and  $\langle 8 \rangle$  but any attempt to find it was unsuccessful. Indeed, phases like  $\langle 5^4 7^4 \rangle$ ,  $\langle 5^3 6^3 7^2 \rangle$  and  $\langle 10^2 7^4 \rangle$  have a zero temperature energy higher than, even though very close to, the regular stripe phases  $\langle 6 \rangle$  or  $\langle 8 \rangle$  in the lattice  $48 \times 48$ : one has to conclude that the size of the lattice under investigation is too *small* to support irregular stripe configurations of the type  $\langle \sim h \rangle$  with  $h \geq 7$ . To check this statement, an investigation on a SQ lattice  $32 \times 32$  for which the consistent regular stripe phases are characterized by  $h = 1, 2, 4, 8, 16$  was performed: a phase  $\langle 3^9 5 \rangle = \langle \sim 3 \rangle$  becomes stable in the region

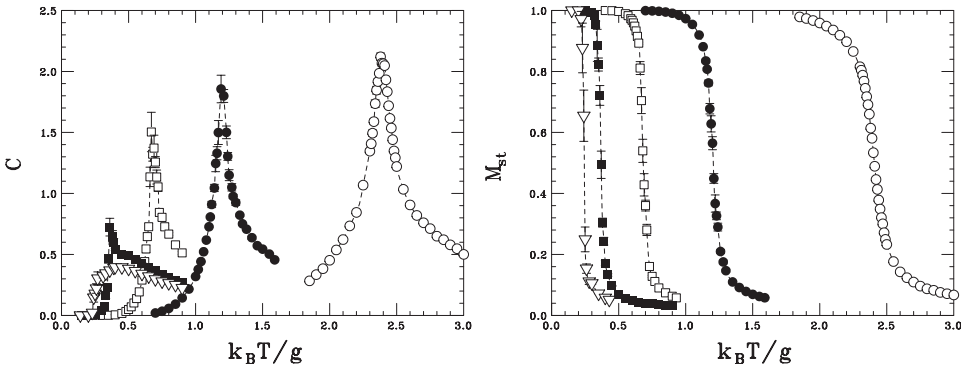


Fig. 10.5. Specific heat (left) and staggered magnetization (right) versus temperature for the Néel (N) antiferromagnet on a SQ lattice  $48 \times 48$ :  $J/g = 0$  (open circles),  $J/g = 0.5$  (full circles),  $J/g = 0.7$  (open squares),  $J/g = 0.8$  (full squares) and  $J/g = 0.83$  (open downward triangles). All MC data is the result of an average over eight independent runs.

$4.56 < J/g < 5.41$  between the stripe phases  $\langle 2 \rangle$  and  $\langle 4 \rangle$  and a phase  $\langle 5^4 6^2 \rangle$  becomes stable for  $6.77 < J/g < 7.99$  between the stripe phases  $\langle 4 \rangle$  and  $\langle 8 \rangle$ . We stress that all irregular stripe phases are unstable in the infinite lattice. For this reason, the detailed investigation of the checkerboard and the stripe phases at finite temperature will be restricted to  $n \leq 3$  and  $h \leq 4$  respectively. Note that for checkerboard phases  $\langle 1, n \rangle$  with  $n > 8$ , the region of stability is so narrow that it cannot be shown within the numerical precision of Table 10.4. The “largest” stripe configuration at zero temperature supported by the lattice  $48 \times 48$  is the stripe phase  $\langle 24 \rangle$  and the phase boundary between it and the F phase is given in Table 10.4:  $J/g = 17.27$ .

In Fig. 10.5, we show the specific heat  $C$  (left panel) and the staggered magnetization  $M_{st}$  (right panel) versus temperature for selected values of  $J/g$  in the range  $0 \leq J/g \leq 0.83$  (N phase). The peak in the specific heat and the drop in the order parameter point out the existence of a phase transition. As one can see from the left panel of Fig. 10.5, both the height of the peak of the specific heat and the transition temperature decrease as  $J/g$  increases: the Néel temperature is  $k_B T_N/g = 2.38, 1.19, 0.67, 0.36$  for  $J/g = 0, 0.5, 0.7, 0.8$ , respectively. Moreover, the shape of the peak becomes increasingly sharper when approaching the boundary between the N and the  $\langle 1, 2 \rangle$  phase ( $J/g = 0.83$ ). Correspondingly, the slope of the staggered magnetization curves at  $T_N$  increases going from  $J/g = 0$  to  $0.83$  as shown in the right panel of Fig. 10.5. All the MC data presented in Fig. 10.5 are obtained averaging over eight independent MC runs. The sharpening of the peak and the increment of the error bars of the data around the transition temperature approaching the phase boundary N– $\langle 1, 2 \rangle$ , seems to point out a change in the order of the phase transition. Indeed, the peak of the specific heat grows as  $L^2$  in a first-order phase transition while it grows “only” as  $\ln L$  in a second-order (continuous) phase transition of a 2D Ising model.<sup>113</sup> Moreover, the “critical region” is absent in a first-order phase transition, leading to a narrowing of the peak itself. Even though a finite-size scaling is not presented here, the second-order character of the

transition can be checked for  $0 < J/g \lesssim 0.5$ . The large error bars for  $J/g \gtrsim 0.5$  are due to the small change in the location of the peak of the specific heat going from one run to another. Indeed, one finds a sharp peak in the specific heat in *each run* whose location and height, however, fluctuate from one run to another, indicating that MC runs of  $10^5$  MCSs are too “short” to reach the equilibrium. Incidentally, much longer runs ( $10^6$  MCSs) also do not give significantly better results. The fluctuation in the location of the peak causes a drastic reduction of the height of the peak itself when an average over eight runs is taken. This drawback does not affect a second-order phase transition as illustrated in Fig. 10.5 looking at the specific heat of the models with  $J/g = 0$  and 0.5. Because of the impossibility of performing much longer MC runs, we investigate the order of the phase transition by looking at the energy and the order parameter density distribution obtained from a single MC run.

In Fig. 10.6, we show the specific heat  $C$ , the staggered magnetization  $M_{st}$  versus temperature for  $J/g = 0.83$  together with the energy density distribution  $P(E)$  and the order parameter density distribution  $P(M_{st})$  for selected temperatures. A sharp peak in the specific heat and a sudden drop in the staggered magnetization is seen at  $k_B T/g = 0.27$ . Correspondingly, a two-peak profile in  $P(E)$  and an intricate structure in  $P(M_{st})$  are seen at the same temperature. Out of  $k_B T/g = 0.27$ , a single

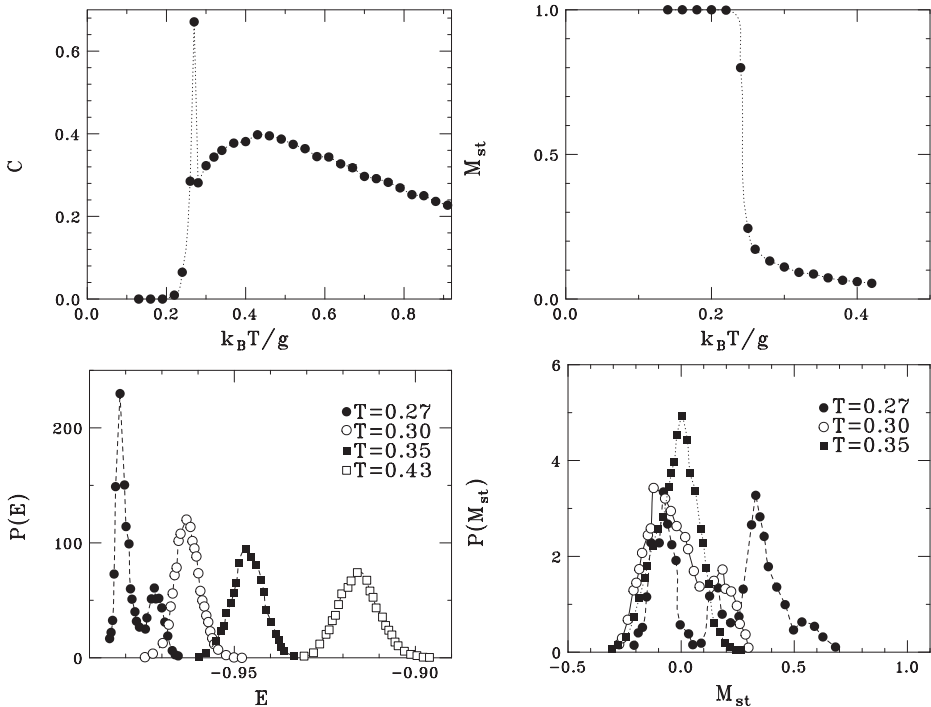


Fig. 10.6. Specific heat (upper left) and order parameter (upper right) versus temperature for  $J/g = 0.83$  (Néel phase). Energy density distribution  $P(E)$  (lower left) and order parameter density distribution  $P(M_{st})$  (lower right) for selected temperatures obtained from a single MC run.



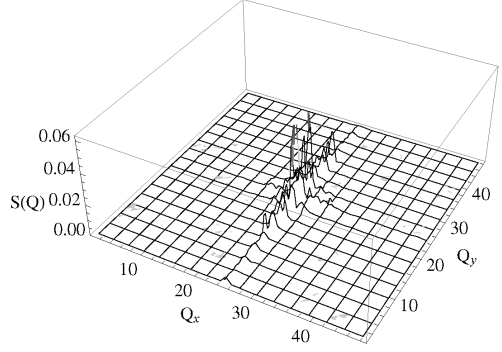
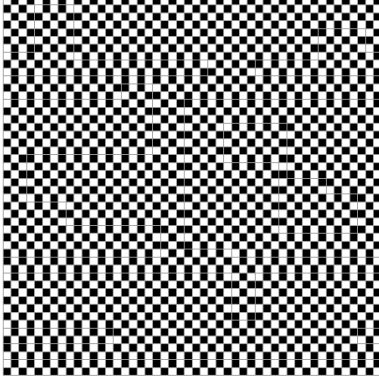
peak structure is recorded. In particular, for  $k_B T/g \leq 0.23$ , the single  $\delta$ -like peak in  $P(M_{\text{st}})$  is located at  $E = -0.986$  and the single peak in  $P(M_{\text{st}})$  is located at  $M_{\text{st}} = 1$ . These values are indistinguishable from their homologous at  $T = 0$ . For  $k_B T/g \geq 0.30$ , a single peak structure reappears: by increasing the temperature, the peak in  $P(E)$  moves smoothly towards higher energy and broadens while the peak in  $P(M_{\text{st}})$  broadens without moving away from the origin. For  $k_B T/g \leq 0.23$ , the structure factor  $\langle S(\mathbf{Q}) \rangle$  shows a  $\delta$ -like peak of intensity  $\simeq 1$  located at  $\mathbf{Q} = (\pi, \pi)$  as expected for the N antiferromagnet. At  $k_B T/g = 0.24$ , the height of the peak reduces to 0.65 without changing location. In the narrow range  $0.25 < k_B T/g < 0.27$ , a ridge-like structure appears around the peak at  $\mathbf{Q} = (\pi, \pi)$  whose intensity is suddenly reduced to 0.09. Both the snapshots of Fig. 10.7 are taken at  $k_B T/g = 0.27$ . The microscopic spin configurations are shown on the left while the corresponding structure factor  $S(\mathbf{Q})$  is shown on the right. The value and the location of the maximum of  $S(\mathbf{Q})$ , the order parameter  $O_{hv}$ , the staggered magnetization  $M_{\text{st}}$  and the energy per spin in units of dipolar interaction  $E$  are recorded over each snapshot. The energy and the staggered magnetization of the upper snapshot correspond approximately to the location of first peak on the left of both  $P(E)$  and  $P(M_{\text{st}})$  at  $k_B T/g = 0.27$  as shown in Fig. 10.6. The energy and the staggered magnetization of the lower snapshot correspond approximately to the second peak of  $P(E)$  and  $P(M_{\text{st}})$  of Fig. 10.6. A mixing of  $\langle 1, 1 \rangle$  and  $\langle 1, 2 \rangle$  domains leading to “incommensurate peaks” located neither at  $\mathbf{Q} = (\pi, \pi)$  (N phase) nor at  $\mathbf{Q} = (\pi, \frac{\pi}{2})$ ,  $(\pi, \frac{3\pi}{2}) \equiv (\pi, -\frac{\pi}{2})$  ( $\langle 1, 2 \rangle$  phase) can be caught looking at the snapshots shown in Fig. 10.7. The domain structure is in turn responsible for the ridge-like profile in the structure factors.

In Fig. 10.8, we show the same quantities as Fig. 10.6 for  $J/g = 0.86$  ( $\langle 1, 2 \rangle$  checkerboard phase) except that the staggered magnetization  $M_{\text{st}}$  has been replaced by the order parameter  $O_{hv}$  given by Eq. (10.4.3). The specific heat shows a pointed peak at  $k_B T/g = 0.34$  where the order parameter drops suddenly to zero. As one can see, the value of the order parameter at  $T = 0$  for the checkerboard phase  $\langle 1, 2 \rangle$  is  $\frac{1}{3}$ . The energy density distribution of Fig. 10.8 shows a single-peak profile at any temperature except at  $k_B T/g = 0.34$  where a broad structure occurs: no two-peak structure, typical of a first-order phase transition, can be seen. The same indication comes from the order parameter density distribution.

In Fig. 10.9, three snapshots taken at  $k_B T/g = 0.34$  ( $J/g = 0.86$ ) are shown with the corresponding structure factors. The upper and lower snapshots are reminiscent of the checkerboard phase  $\langle 1, 2 \rangle$  and  $\langle 2, 1 \rangle$  respectively: the simultaneous presence of these two configurations points out the occurrence of a phase in which the orientational order is lost and the checkerboard configurations rotate freely from  $\langle 1, 2 \rangle$  to  $\langle 2, 1 \rangle$  phase. The middle snapshot shows a configuration with a marked domain-structure and a ridge-like profile in the structure factor. Note that in all snapshots, the height of the peaks in the structure factors are no more than 20% of the corresponding peaks at  $T = 0$ .

Figure 10.10 shows the specific heat (left) and the order parameter (right) versus temperature for several  $J/g$  in the range  $0.88 < J/g < 2.52$  ( $\langle 1 \rangle$  phase). For  $J/g$

$$S\left(\pi, \frac{19\pi}{24}\right) = 0.091, \quad O_{hv} = \frac{n_h - n_v}{n_h + n_v} = 0.107, \quad M_{st} = -0.107, \quad E = -0.980$$



$$S\left(\pi, \frac{11\pi}{12}\right) = 0.062, \quad O_{hv} = \frac{n_h - n_v}{n_h + n_v} = 0.063, \quad M_{st} = 0.109, \quad E = -0.972$$

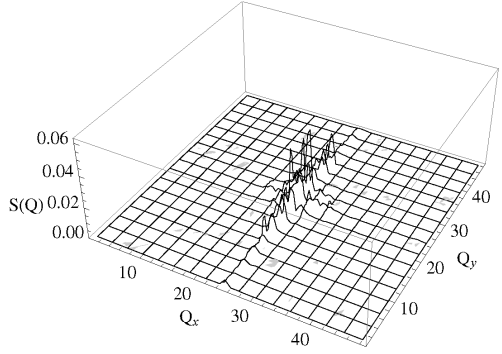
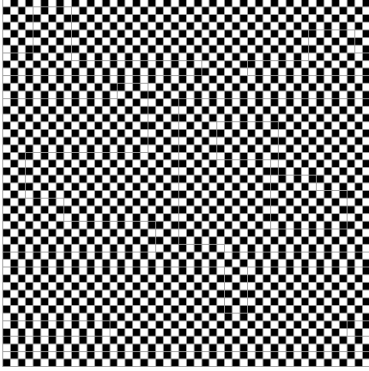


Fig. 10.7. Snapshots and corresponding structure factors for  $J/g = 0.83$  (Néel phase) and  $k_B T/g = 0.27$ . The values of the maximum of the structure factor and of  $O_{hv}$ ,  $M_{st}$  and  $E$  are indicated over each snapshot.  $\mathbf{Q} = (\frac{2m\pi}{48}, \frac{2n\pi}{48})$  with  $n, m = 0, 1, \dots, 47$ .

close to the phase boundary between the stripe  $\langle 1 \rangle$  and the checkerboard  $\langle 1, 2 \rangle$  (full circle curves) and for  $J/g$  near to the boundary between the stripe phases  $\langle 1 \rangle$  and  $\langle 2 \rangle$  (open upward triangle curves), the specific heat shows a narrow peak and the order parameter a sudden drop. Moving away from the boundaries towards the centre of the existence region of the phase  $\langle 1 \rangle$ , the peak in the specific heat broadens and the slope of the drop in the order parameter decreases. Note that the error bars entered by the average over eight independent runs grow when approaching the boundaries.

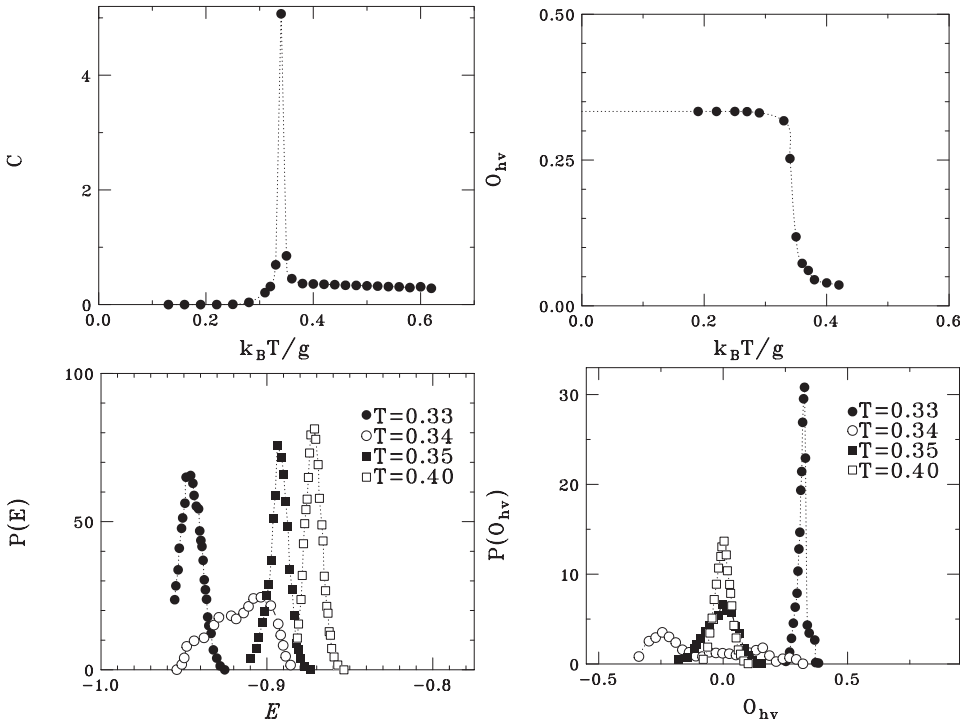
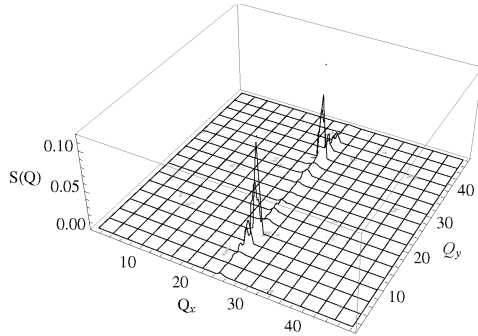
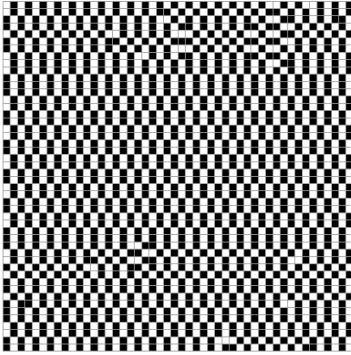


Fig. 10.8. Specific heat (upper left) and order parameter (upper right) versus temperature for  $J/g = 0.86$  ( $\langle 1, 2 \rangle$  phase). Energy density distribution  $P(E)$  (lower left) and order parameter density distribution  $P(O_{hv})$  (lower right) for selected temperatures.

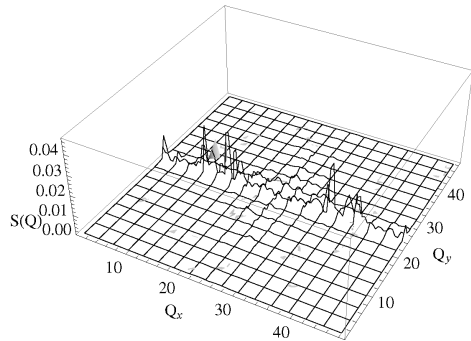
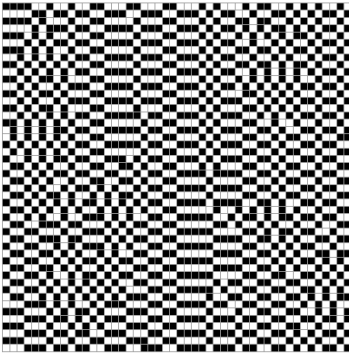
In Fig. 10.11, we show the specific heat, the order parameter, the energy and the order parameter density distribution for  $J/g = 2.5$  ( $h = 1$ ) as obtained from a single MC run. At  $k_B T/g = 0.53$ , the specific heat shows a sharp peak and the order parameter a single large step from  $O_{hv} \simeq 1$  corresponding to the low temperature stripe configuration to  $O_{hv} \sim 0$  corresponding to the high temperature paramagnetic phase. At the same time, the energy density distribution (lower left panel of Fig. 10.11) shows a shift in the location of the peak going from  $k_B T/g = 0.52$  (full circles) to  $0.54$  (full squares). However, at  $k_B T/g = 0.53$  (open circles), any structure is hard to be identified. Notice the smooth displacement of the peak towards higher energy when increasing the temperature from  $k_B T/g = 0.54$ . A similar behaviour is found in the order parameter density distribution  $P(O_{hv})$  (lower right panel of Fig. 10.11): a shift from the sharp peak centred at  $O_{hv} = -1$  at  $k_B T/g = 0.52$  to the broad peak centred at  $O_{hv} = 0$  at  $k_B T/g = 0.6$  is clearly seen. A very flat profile is observed at  $k_B T/g = 0.54$ .

In Fig. 10.12, we show two snapshots taken at  $k_B T/g = 0.53$ . The upper snapshot corresponds to a stripe configuration  $\langle 1 \rangle$  while the lower snapshot corresponds to a “tetragonal” phase<sup>112</sup> where the orientational order is lost. As one can see looking at the corresponding structure factor profiles, the stripe phase  $\langle 1 \rangle$  is characterized

$$S\left(\pi, \frac{\pi}{2}\right) = 0.122, \quad O_{hv} = \frac{n_h - n_v}{n_h + n_v} = 0.301, \quad E = -0.940$$



$$S\left(\frac{9\pi}{24}, \pi\right) = 0.048, \quad O_{hv} = \frac{n_h - n_v}{n_h + n_v} = -0.200, \quad E = -0.910$$



$$S\left(\frac{11\pi}{24}, \pi\right) = 0.114, \quad O_{hv} = \frac{n_h - n_v}{n_h + n_v} = -0.303, \quad E = -0.931$$

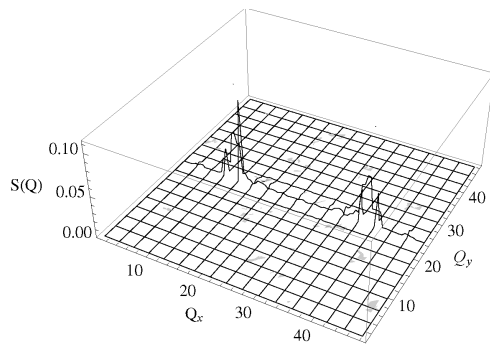
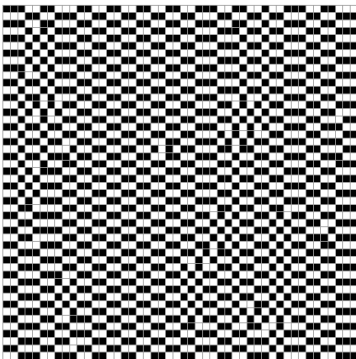


Fig. 10.9. Snapshots and corresponding structure factors for  $J/g = 0.86$  ( $(1,2)$  checkerboard phase) and  $k_B T/g = 0.34$ . The values of the maximum of the structure factor and of  $O_{hv}$  and  $E$  are indicated over each snapshot.

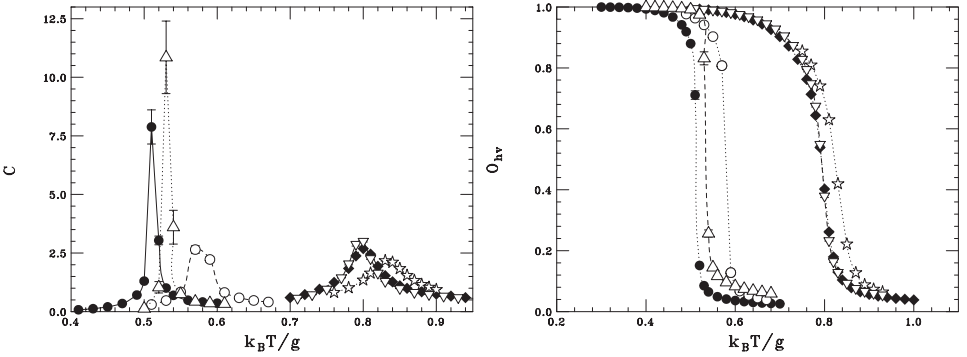


Fig. 10.10. Specific heat (left) and order parameter (right) versus temperature in the stripe phase with  $h = 1$  for several  $J/g$ :  $J/g = 0.95$  (full circles),  $J/g = 1$  (open circles),  $J/g = 1.4$  (full diamonds),  $J/g = 1.7$  (open stars),  $J/g = 2$  (open downward triangles) and  $J/g = 2.5$  (open upward triangles). All MC data is obtained from an average of eight independent runs.

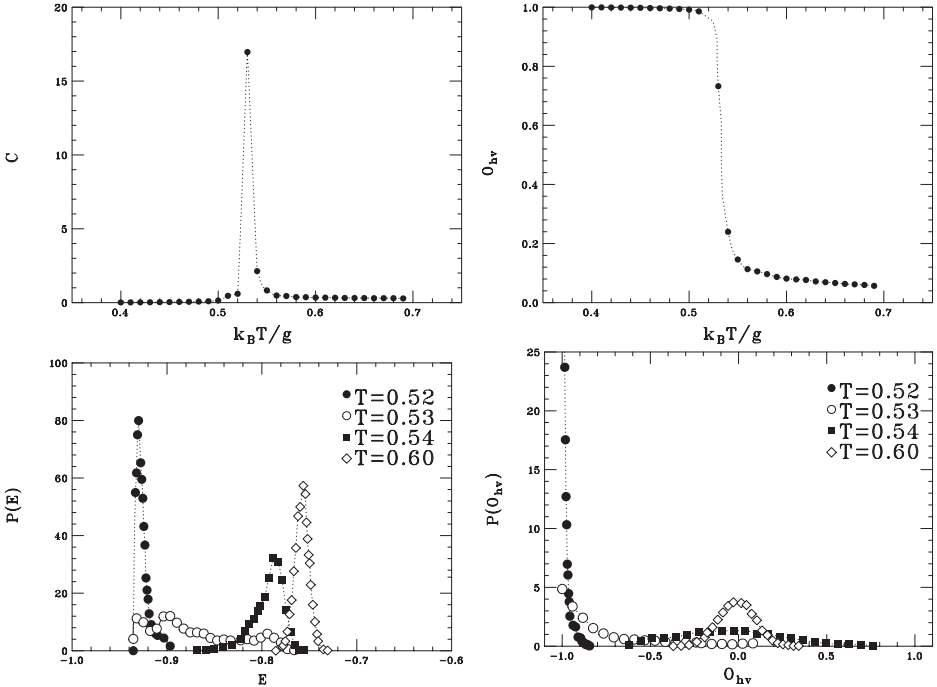
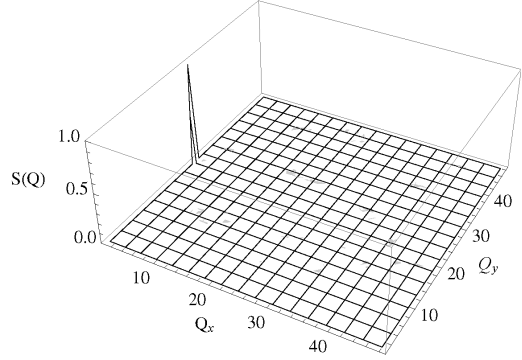
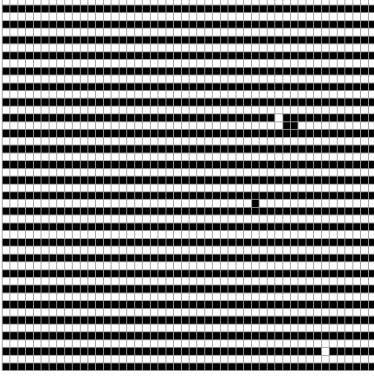


Fig. 10.11. Specific heat (upper left) and order parameter (upper right) versus temperature for  $J/g = 2.5$  ((1) phase). Energy density distribution  $P(E)$  (lower left) and order parameter density distribution  $P(O_{hv})$  (lower right) for selected temperatures. All MC data are obtained from a single MC run.

by a  $\delta$ -like peak at the “commensurate” wavevector  $\mathbf{Q} = (0, \pi)$  while the tetragonal phase is characterized by a crown-shaped profile.<sup>102</sup> These two snapshots, taken at  $k_B T/g = 0.53$ , point out the coexistence of the stripe configuration (1) with the disordered phase. Their energies correspond approximately to the left and right limit

$$S(0, \pi) = 0.991, \quad O_{hv} = \frac{n_h - n_v}{n_h + n_v} = -0.993, \quad E = -0.930$$



$$O_{hv} = \frac{n_h - n_v}{n_h + n_v} = 0.022, \quad E = -0.780$$

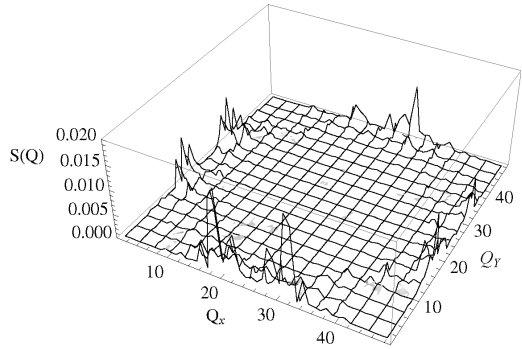
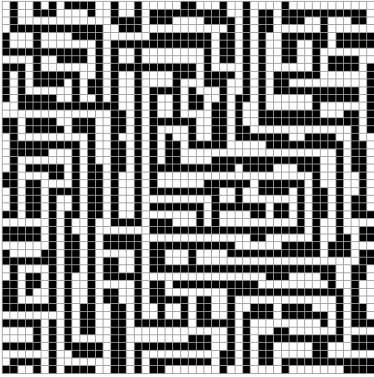


Fig. 10.12. Snapshots and corresponding structure factors for  $J/g = 2.5$  (stripe phase with  $h = 1$ ) and  $k_B T/g = 0.53$ . The values of the maximum of the structure factor and of the observables  $O_{hv}$  and  $E$  are indicated over each snapshot.

of the flat profile seen in the lower left panel of Fig. 10.11 for  $k_B T/g = 0.53$ . Many other snapshots were taken: those with an energy  $-0.93 \lesssim E \lesssim -0.81$  are similar to the upper snapshot even though some labyrinth disorder begins to appear, leading to a decrease of the height of the commensurate peak from 1 to  $\sim 0.3$ ; on the contrary, those with an energy  $-0.81 \lesssim E \lesssim -0.78$  are very similar to the lower snapshot since the labyrinth disorder spreads on the whole lattice (tetragonal phase). The crown-shape of the structure factor remains for higher temperatures: the peak in  $P(E)$  of Fig. 10.11 that moves smoothly to higher energy for  $k_B T/g \geq 0.54$  corresponds to the tetragonal phase. The labyrinth shape of the tetragonal configuration differs from the pattern of the usual paramagnetic configuration which is recovered, however, at higher temperatures.

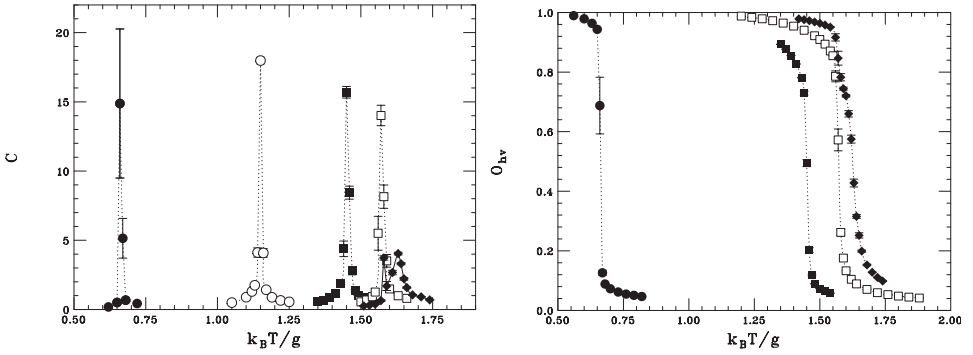


Fig. 10.13. Specific heat (left) and order parameter (right) versus temperature in the stripe phase with  $h = 2$  for several  $J/g$ :  $J/g = 2.6$  (full circles),  $J/g = 3$  (open circles),  $J/g = 3.4$  (full squares),  $J/g = 3.7$  (open squares) and  $J/g = 4$  (full diamonds).

In Fig. 10.13, we show the specific heat (left) and the order parameter (right) versus temperature for several  $J/g$  in the range  $2.52 < J/g < 4.34$  (phase  $\langle 2 \rangle$ ). The peaks in the specific heat are sharp and the drops of the order parameter are sudden over the whole region of existence except very close to the phase boundary with the stripe phase  $\langle 3 \rangle$  where a narrow peak followed by a wider one in the specific heat and a finite slope in the order parameter are clearly seen. To understand this different behaviour close to the boundaries, we investigate the systems with  $J/g = 2.6$  and  $4.3$  in more detail.

In Fig. 10.14, we show the specific heat, the order parameter, the energy and order parameter density distribution for  $J/g = 2.6$ . A sharp peak in the specific heat and a sudden drop of the order parameter are observed at  $k_B T/g = 0.66$ . Correspondingly, a two-peak structure in both  $P(E)$  and  $P(O_{hv})$  is seen at the same temperature. The snapshots taken at  $k_B T/g = 0.66$ , shown in Fig. 10.15, indicate the coexistence of the phase  $\langle 2 \rangle$  (upper snapshot) with the tetragonal phase (lower snapshot) which looks very similar to the lower snapshot of Fig. 10.12.

The MC simulation for  $J/g = 4.3$  leads to a different scenario as shown in Fig. 10.16. The specific heat shows two narrow peaks at  $k_B T/g = 1.42$  and  $1.48$  and a broad one around  $k_B T/g = 1.65$ . The order parameter shows two small steps in correspondence of the two sharp peaks of the specific heat and a smooth decrease around  $k_B T/g = 1.65$ . The energy and the order parameter density distributions show a two-peak structure at  $k_B T/g = 1.42$  and  $1.48$ . The two snapshots of Fig. 10.17 taken at  $k_B T/g = 1.42$  show the coexistence of the stripe phase  $\langle 2 \rangle$  with peaks in the structure factor at  $\mathbf{Q} = (0, \pm \frac{\pi}{2})$  and a *modulated* phase with peaks at the incommensurate wavevectors  $\mathbf{Q} = (0, \pm \frac{11}{24}\pi)$ . As previously explained, the occurrence of peaks in the structure factor in correspondence of incommensurate wavevectors reflects a mixing of two defected stripe phases with different  $h$ : in the present case, the stripe phases  $\langle 2 \rangle$  and  $\langle 3 \rangle$ . Analogously, the two snapshots of Fig. 10.18 taken at  $k_B T/g = 1.48$  point out the coexistence of two different incommensurate phases with peaks at  $\mathbf{Q} = (0, \pm \frac{11}{24}\pi)$  (upper snapshot) and

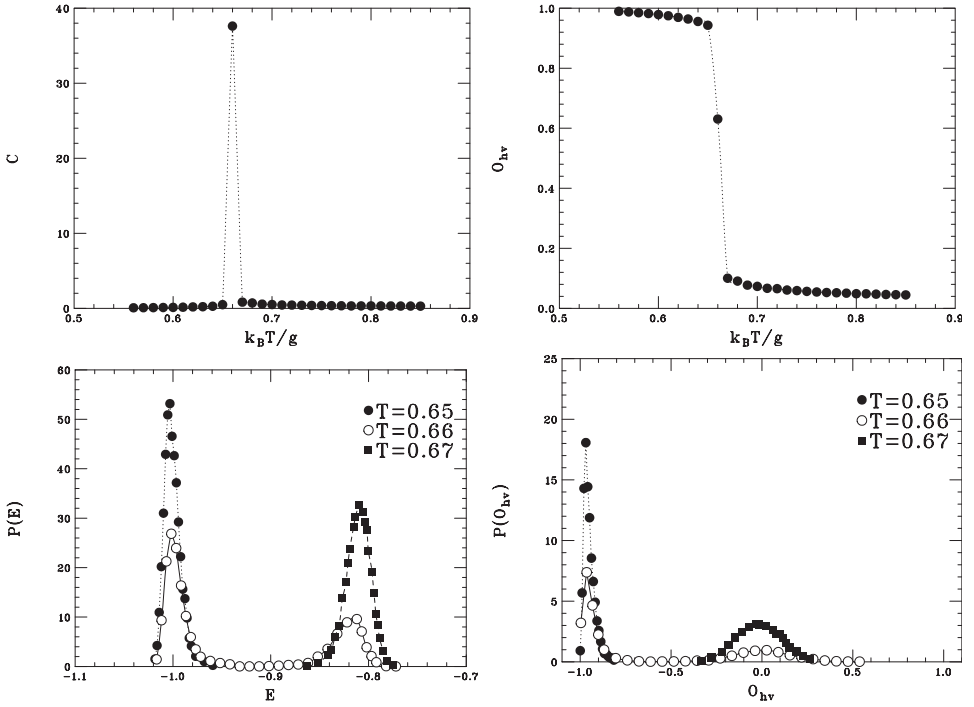
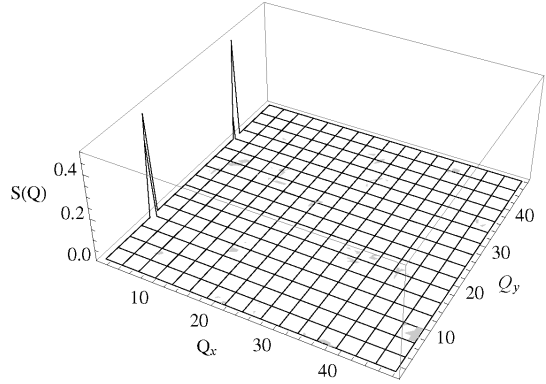
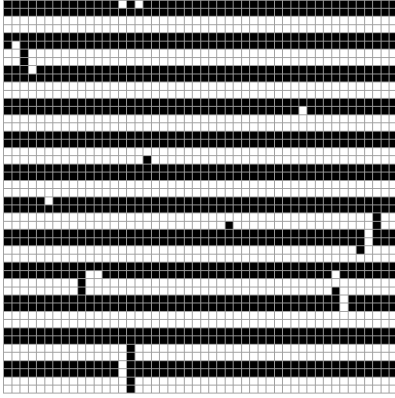


Fig. 10.14. Specific heat (upper left) and order parameter (upper right) versus temperature for  $J/g = 2.6$  ( $\langle 2 \rangle$  phase). Energy density distribution  $P(E)$  (lower left) and order parameter density distribution  $P(O_{hv})$  (lower right) for selected temperatures.

$\mathbf{Q} = (0, \pm \frac{10}{24}\pi)$  (lower snapshot), respectively. The weight of the phase  $\langle 3 \rangle$  increases and the incommensurate wavevectors move towards those characterizing the stripe  $\langle 3 \rangle$ :  $\mathbf{Q} = (0, \pm \frac{\pi}{3})$ . Finally, the three snapshots of Fig. 10.19 taken at  $k_B T/g = 1.65$  indicate the existence of a tetragonal phase without orientational order<sup>102</sup> in which the stripes rotate freely (upper and lower snapshots). The labyrinth shape of the middle snapshot and the corresponding crown-shaped structure factor profile is similar to the analogous snapshots of Figs. 10.12 and 10.15. The snapshots of Figs. 10.17–10.19 allow us to understand the density distributions of Fig. 10.16. The two-peak structure of both the energy and the order parameter density distribution at  $k_B T/g = 1.42$  points out a first-order phase transition between the commensurate (C) stripe phase  $\langle 2 \rangle$  and the incommensurate phase  $I_1$  characterized by  $\mathbf{Q} = (0, \pm \frac{11}{24}\pi)$ . Similarly, the two-peak structure at  $k_B T/g = 1.48$  points out a transition between the incommensurate phases  $I_1$  and  $I_2$ , the latter being characterized by  $\mathbf{Q} = (0, \pm \frac{10}{24}\pi)$ . The transition C– $I_1$  is almost certainly a true phase transition whereas the transition  $I_1$ – $I_2$  is almost certainly a finite-size effect: indeed, for any finite lattice, any change in the wavevector  $\mathbf{Q}$  may occur only by discrete steps  $\Delta\mathbf{Q} = \frac{2\pi}{L}$  as well as any change in the corresponding energy (leading to repeated narrow peaks in the specific heat) and in the order parameter (repeated small steps in  $O_{hv}$ ). Most probably, the modulated phase is a genuine one but the



$$S\left(0, \frac{\pi}{2}\right) = 0.475, \quad O_{hv} = \frac{n_h - n_v}{n_h + n_v} = -0.906, \quad E = -0.993$$



$$O_{hv} = \frac{n_h - n_v}{n_h + n_v} = 0.011, \quad E = -0.815$$

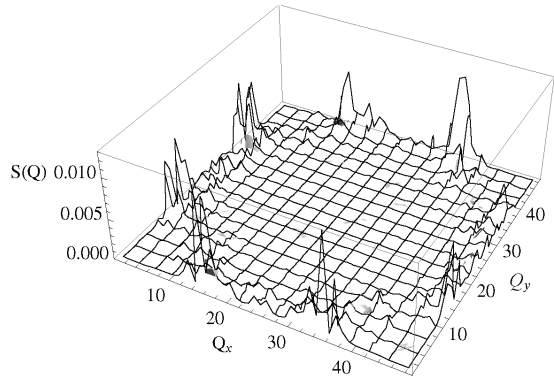
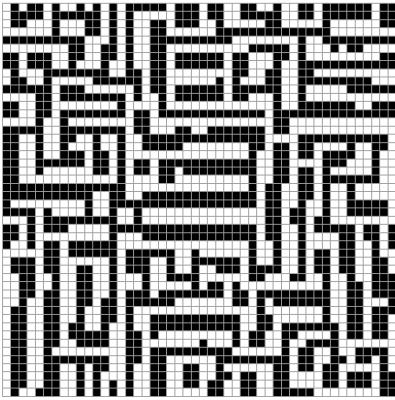


Fig. 10.15. Snapshots and corresponding structure factors for  $J/g = 2.6$  (stripe phase with  $h = 2$ ) and  $k_B T/g = 0.66$ . The values of the maximum of the structure factor and of the observables  $O_{hv}$  and  $E$  are indicated over each snapshot.

incommensurate wavevector  $Q$  changes continuously and not by steps for a lattice with  $L \rightarrow \infty$ .

What about the existence of LRO in the modulated phase and the order of the phase transition? No proof exists for the existence of LRO in the modulated phase: if the LRO is absent, the true phase transition occurs at the first peak of the specific heat, otherwise the first peak corresponds to a transition between two ordered phases and only in the proximity of the broad peak, an order–disorder transition occurs. This second hypothesis seems less realistic than the first one since no peak is seen at the “second” transition. A more realistic scenario is to think of the

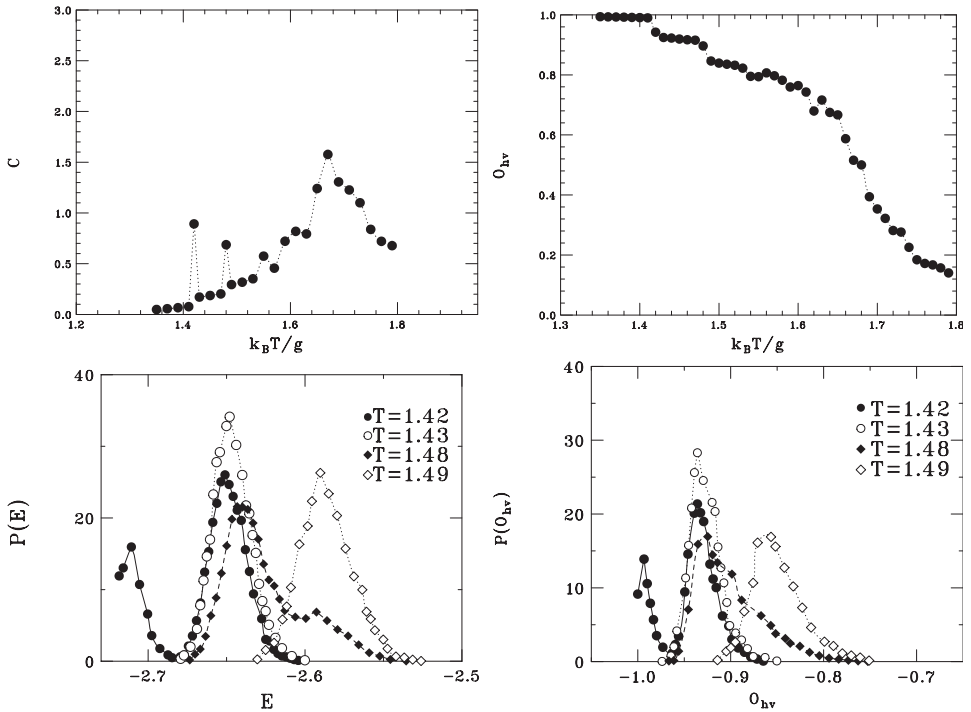


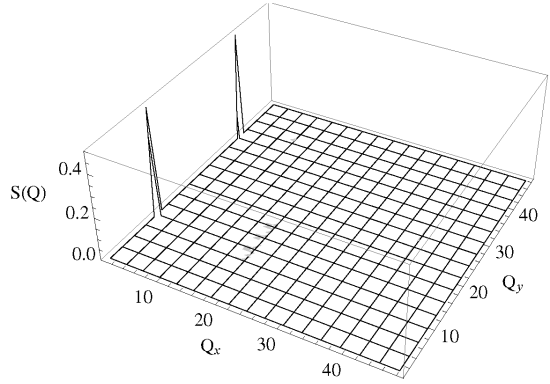
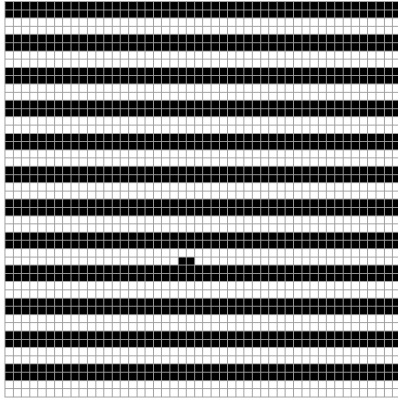
Fig. 10.16. Specific heat (upper left) and order parameter (lower left) versus temperature for  $J/g = 4.3$  ( $\langle 2 \rangle$  phase). Energy density distribution  $P(E)$  (upper right) and order parameter density distribution  $P(O_{hv})$  (lower right) for selected temperatures.

modulated phase as a BKT phase<sup>89</sup> in which the LRO is absent but the correlation functions decay algebraically with distance, in contrast with the paramagnetic phase where the correlations decay exponentially. In this case, two transitions occur: C–I (stripe-modulated phase) and I–P (modulated-paramagnetic phase). The transition between the BKT and the paramagnetic phase does not imply the existence of a sharp peak in the specific heat. In any case, the occurrence of the modulated phase seems well established.

The specific heat and the order parameter corresponding to the stripe phase  $\langle 3 \rangle$  ( $4.34 < J/g < 5.63$ ) are shown in Fig. 10.20. The two peaks in the specific heat are seen only near to the phase boundaries  $\langle 2 \rangle - \langle 3 \rangle$  and  $\langle 3 \rangle - \langle 4 \rangle$  respectively.

In Fig. 10.21, the specific heat, the order parameter and their density distributions are shown for  $J/g = 4.4$ . A sharp peak in the specific heat and a small step in the order parameter are clearly seen at  $k_B T/g = 1.52$ . Moreover, one can see a broad peak in the specific heat at  $k_B T/g = 1.69$  and a corresponding smooth decrease of the order parameter around the same temperature. The energy density distribution shows a peak followed by a shoulder at  $k_B T/g = 1.52$  and a well-defined single peak at higher temperature. The order parameter density distribution shows a peak with an imperceptible shoulder at  $k_B T/g = 1.52$  and two symmetric peaks at  $O_{hv} \simeq \pm 0.7$  at  $k_B T/g = 1.69$ , indicating the free rotation of the

$$S\left(0, \frac{\pi}{2}\right) = 0.498, \quad O_{hv} = \frac{n_h - n_v}{n_h + n_v} = -0.997, \quad E = -2.713$$



$$S\left(0, \frac{11\pi}{24}\right) = 0.295, \quad O_{hv} = \frac{n_h - n_v}{n_h + n_v} = -0.952, \quad E = -2.655$$

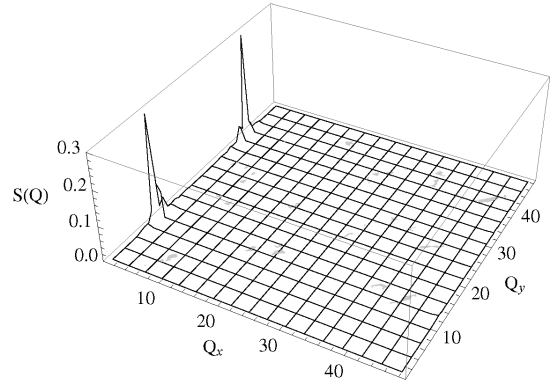
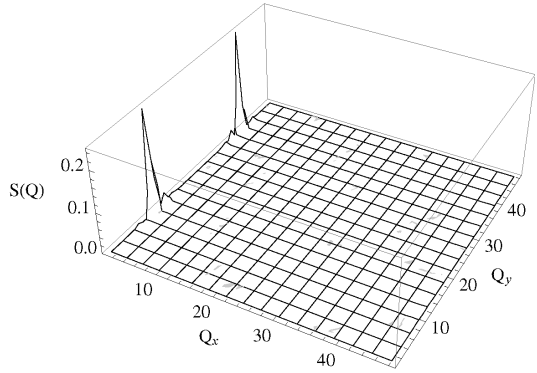
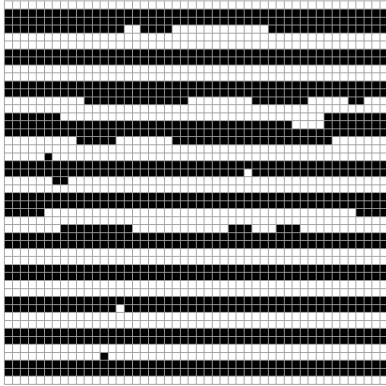


Fig. 10.17. Snapshots and corresponding structure factors for  $J/g = 4.3$  (stripe phase with  $h = 2$ ) and  $k_B T/g = 1.42$ . The values of the maximum of the structure factor and of the observables  $O_{hv}$  and  $E$  are indicated over each snapshot.

stripes. The snapshots of Fig. 10.22 are taken at  $k_B T/g = 1.52$  and show the coexistence of the C-phase  $\langle 3 \rangle$  characterized by three peaks at the wavevectors  $\mathbf{Q} = (0, \pm \frac{\pi}{3})$  and  $(0, \pi)$  (upper snapshot) with an I-phase characterized by two peaks at wavevectors  $\mathbf{Q} = (0, \pm \frac{3}{8}\pi)$  (lower snapshot). Note that in the C-phase  $\langle 3 \rangle$ , the location of the three  $\delta$ -peaks in the profile of the structure factor along with their corresponding heights can be obtained directly from Eq. (10.3.24) at  $T = 0$ . The upper snapshot of Fig. 10.22, even though taken at  $k_B T/g = 1.52$ , looks very similar to the ground-state configuration. The snapshots of Fig. 10.23 are taken at  $k_B T/g = 1.69$  and show the free rotation of the stripes (upper and lower snapshot)

$$S\left(0, \frac{11\pi}{24}\right) = 0.252, \quad O_{hv} = \frac{n_h - n_v}{n_h + n_v} = -0.934, \quad E = -2.642$$



$$S\left(0, \frac{10\pi}{24}\right) = 0.176, \quad O_{hv} = \frac{n_h - n_v}{n_h + n_v} = -0.863, \quad E = -2.599$$

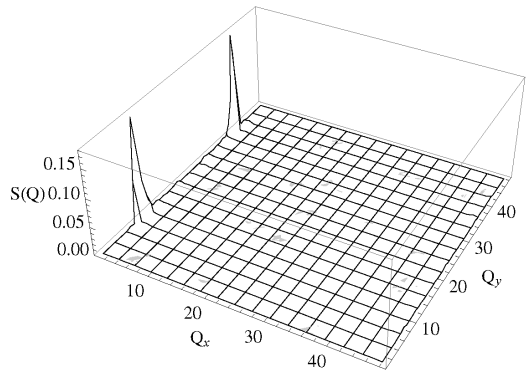
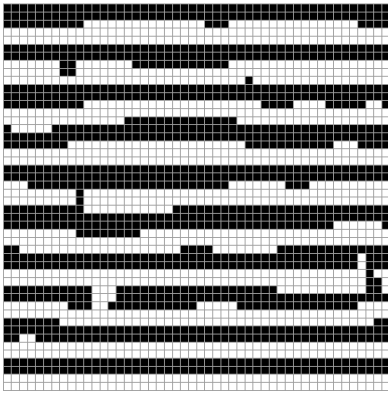
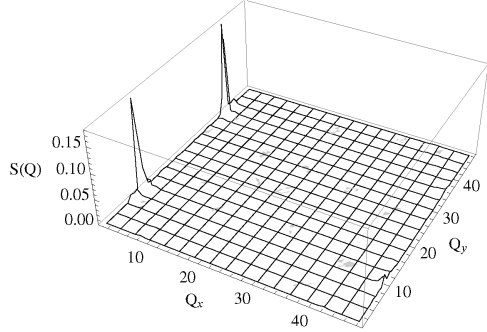
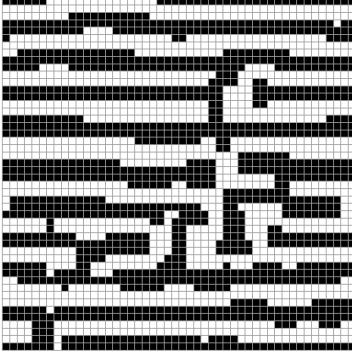


Fig. 10.18. Snapshots and corresponding structure factors for  $J/g = 4.3$  (stripe phase with  $h = 2$ ) and  $k_B T/g = 1.48$ . The values of the maximum of the structure factor and of the observables  $O_{hv}$  and  $E$  are indicated over each snapshot.

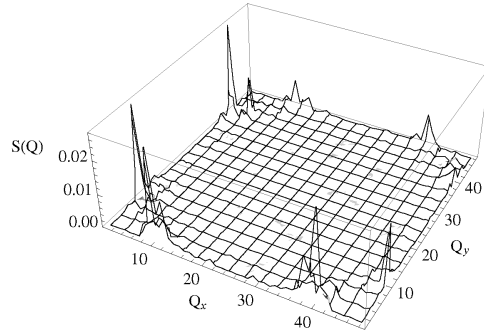
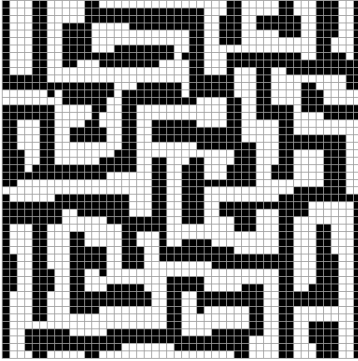
along with the labyrinth configuration (middle snapshot). All these configurations are typical of the tetragonal phase.<sup>112</sup>

The specific heat and the order parameter corresponding to the stripe phases with  $h = 4$  ( $5.63 < J/g < 6.92$ ) are shown in Fig. 10.24. For  $J/g > 17.27$ , where the stable phase is the ferromagnetic (F) one, an interesting behaviour of the specific heat versus temperature is shown in Fig. 10.25 where a two-peak structure is clearly seen for specific heats with  $20 < J/g < 50$ : the low temperature peak is very narrow while the high temperature peak is rather broad. For  $60 < J/g < 100$ , a single peak is seen. For  $J/g = 20$ , the error bars on the height of the first peak are very large because of the uncertainty of the exact location of the temperature at which the

$$S\left(0, \frac{10\pi}{24}\right) = 0.179, \quad O_{hv} = \frac{n_h - n_v}{n_h + n_v} = -0.684, \quad E = -2.490$$



$$S\left(0, \frac{9\pi}{24}\right) = S\left(\frac{9\pi}{24}, 0\right) = 0.028, \quad O_{hv} = \frac{n_h - n_v}{n_h + n_v} = 0.036, \quad E = -2.387$$



$$S\left(\frac{9\pi}{24}, 0\right) = 0.242, \quad O_{hv} = \frac{n_h - n_v}{n_h + n_v} = 0.731, \quad E = -2.514$$

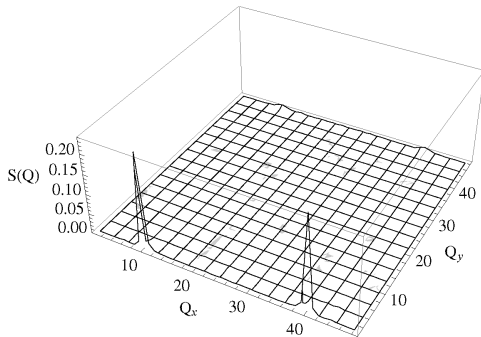
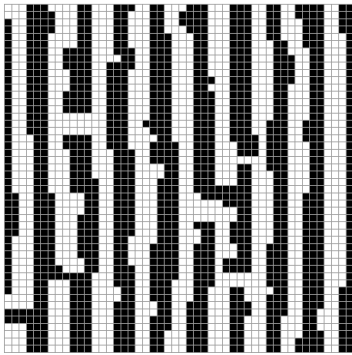


Fig. 10.19. Snapshots and corresponding structure factors for  $J/g = 4.3$  (stripe phase with  $h = 2$ ) and  $k_B T/g = 1.65$ . The values of the maximum of the structure factor and of the observables  $O_{hv}$  and  $E$  are indicated over each snapshot.

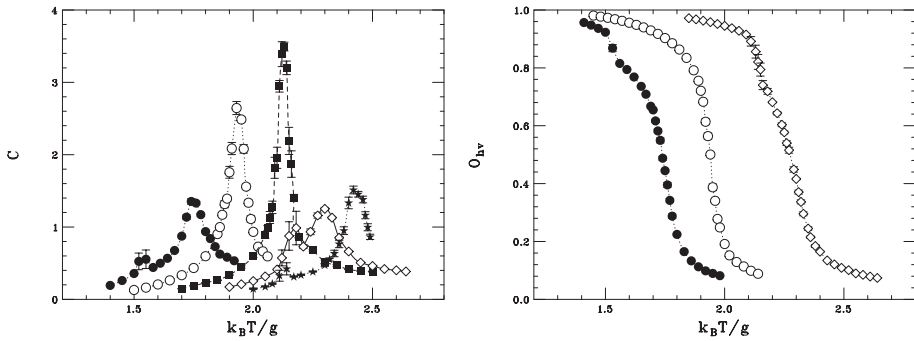


Fig. 10.20. Specific heat versus temperature in the stripe phase with  $h = 3$  for several  $J/g$ :  $J/g = 4.4$  (full circles),  $J/g = 4.7$  (open circles),  $J/g = 5$  (full squares),  $J/g = 5.3$  (open diamonds) and  $J/g = 5.6$  (full stars).

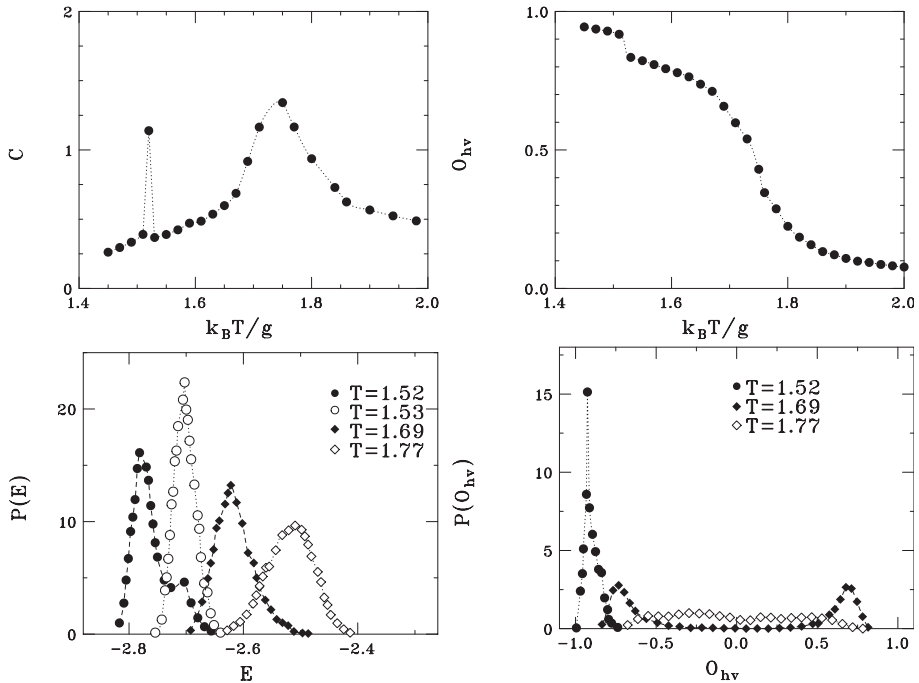
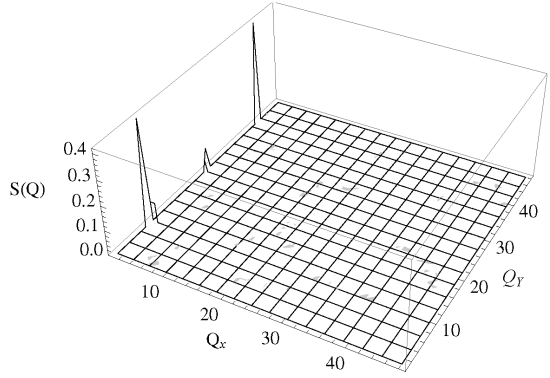
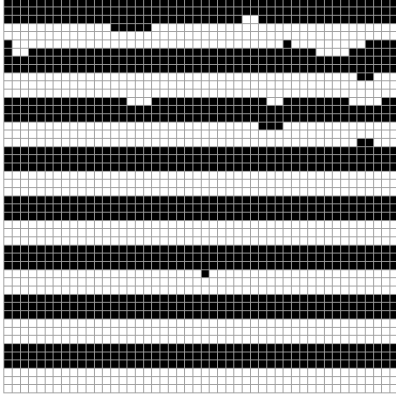


Fig. 10.21. Specific heat (upper left) and order parameter (lower left) versus temperature for  $J/g = 4.4$  ( $\langle 3 \rangle$  phase). Energy density distribution  $P(E)$  (upper right) and order parameter density distribution  $P(O_{hv})$  (lower right) for selected temperatures.

peak occurs. The error bars on the narrow peaks gradually reduce with increasing  $J/g$ . These facts seem to point out the existence of a first-order phase transition between the F and the paramagnetic phase for  $J/g < 50$ . On the contrary, for  $J/g > 50$ , the narrow peak merges into the broad one and a second-order phase transition seems to occur. A least square linear fit of the temperature at which the

$$S\left(0, \frac{\pi}{3}\right) = 0.424, \quad O_{hv} = \frac{n_h - n_v}{n_h + n_v} = -0.935, \quad E = -2.783$$



$$S\left(0, \frac{3\pi}{8}\right) = 0.309, \quad O_{hv} = \frac{n_h - n_v}{n_h + n_v} = -0.845, \quad E = -2.701$$

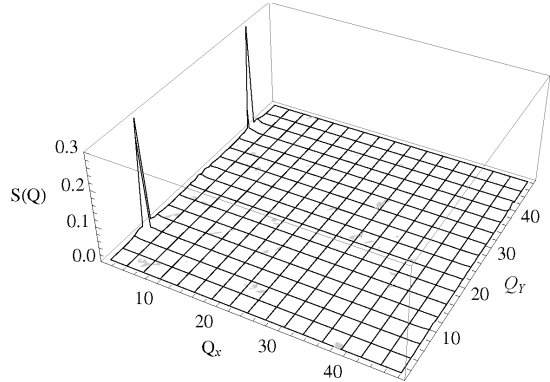
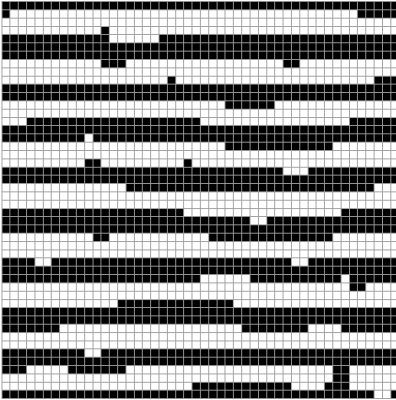


Fig. 10.22. Snapshots and corresponding structure factors for  $J/g = 4.4$  (stripe phase with  $h = 3$ ) and  $k_B T/g = 1.52$ . The values of the maximum of the structure factor and of the observables  $O_{hv}$  and  $E$  are indicated over each snapshot.

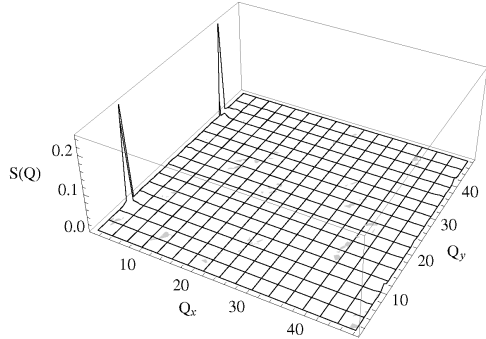
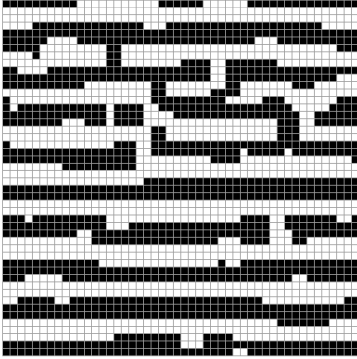
maximum of the specific heat occurs gives

$$k_B T_c = 2.285J - (24.1 \pm 0.4)g. \quad (10.4.4)$$

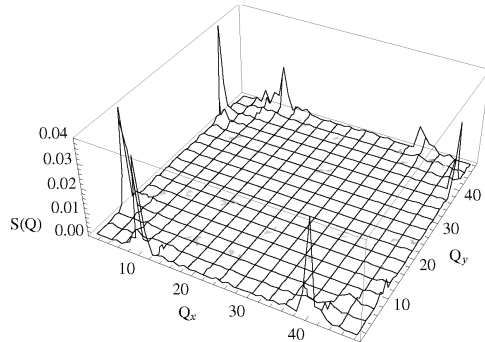
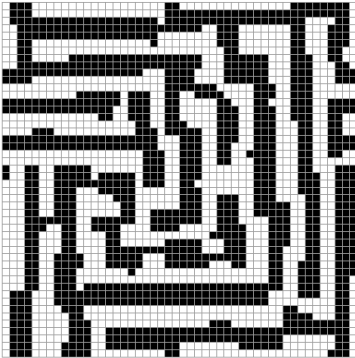
The finite-size correction to the critical temperature for a SQ Ising model with NN exchange interaction was given by Ferdinand and Fisher<sup>115</sup>:

$$k_B T_c(L)/J = 2.269185 + 0.818/L \quad (10.4.5)$$

$$S\left(0, \frac{3\pi}{8}\right) = 0.264, \quad O_{hv} = \frac{n_h - n_v}{n_h + n_v} = -0.701, \quad E = -2.618$$



$$S\left(\frac{3\pi}{8}, 0\right) = S\left(0, \frac{3\pi}{8}\right) = 0.040, \quad O_{hv} = \frac{n_h - n_v}{n_h + n_v} = 0.034, \quad E = -2.537$$



$$S\left(\frac{3\pi}{8}, 0\right) = 0.227, \quad O_{hv} = \frac{n_h - n_v}{n_h + n_v} = 0.708, \quad E = -2.638$$

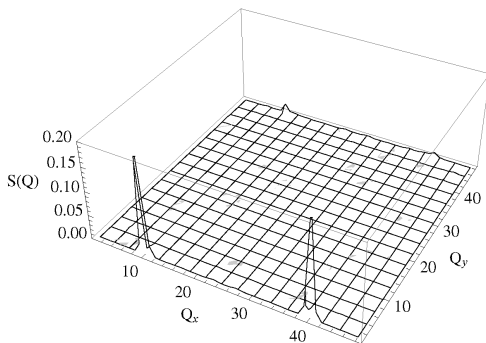
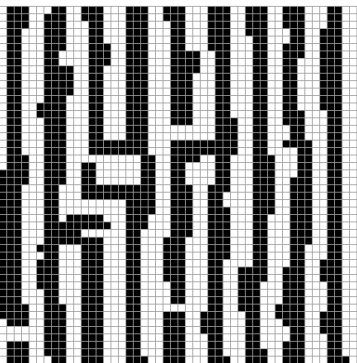


Fig. 10.23. Snapshots and corresponding structure factors for  $J/g = 4.4$  (stripe phase with  $h = 3$ ) and  $k_B T/g = 1.69$ . The values of the maximum of the structure factor and of the observables  $O_{hv}$  and  $E$  are indicated over each snapshot.



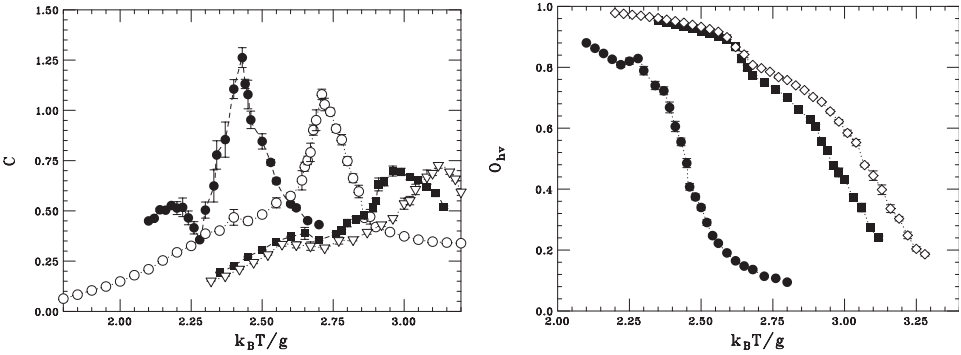


Fig. 10.24. Specific heat versus temperature in the stripe phase with  $h = 4$  for several  $J/g$ :  $J/g = 5.7$  (full circles),  $J/g = 6$  (open circles),  $J/g = 6.5$  (full squares) and  $J/g = 6.6$  (open diamonds).

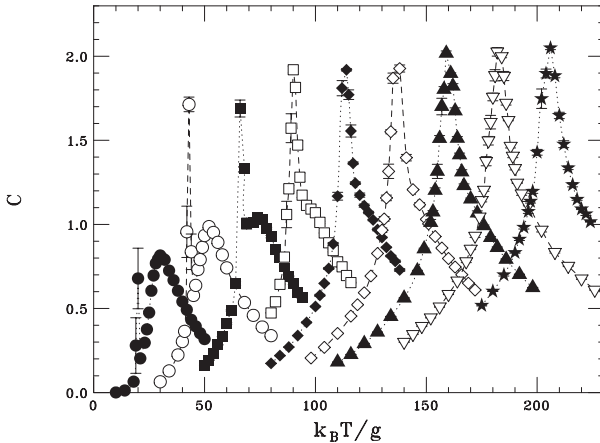


Fig. 10.25. Specific heat versus temperature in the ferromagnetic phase ( $J/g > 17.27$ ) for several  $J/g$ :  $J/g = 20$  (full circles),  $J/g = 30$  (open circles),  $J/g = 40$  (full squares),  $J/g = 50$  (open squares),  $J/g = 60$  (full diamonds),  $J/g = 70$  (open diamonds),  $J/g = 80$  (upward full triangles),  $J/g = 90$  (downward open triangles) and  $J/g = 100$  (full stars).

where  $L$  is the side of the SQ lattice. In the same paper, the authors give the maximum of the specific heat occurring at  $T_c(L)$  as function of  $L$ :

$$C_{\max}(L)/(k_B L^2) = 0.4945386 \ln L + 0.201359. \quad (10.4.6)$$

It is well known that in the thermodynamic limit, the specific heat of the 2D NN Ising model diverges at the critical temperature where it undergoes a second-order phase transition from the ferromagnetic to the paramagnetic phase. For  $L = 48$ , Eqs. (10.4.5) and (10.4.6) give  $k_B T_c(48) = 2.286J$  and  $C_{\max}(48)/(k_B 48^2) = 2.116$ , respectively. For  $J/g \gtrsim 50$ , where the effect of the dipolar interaction is expected to become irrelevant, we see from Fig. 10.25 that the maximum of the specific heat is  $C_{\max} \sim 2.0$ , in agreement with the result of Ferdinand and Fisher<sup>115</sup> that holds, strictly speaking, only for  $J/g \rightarrow \infty$ . One can check the reliability of the

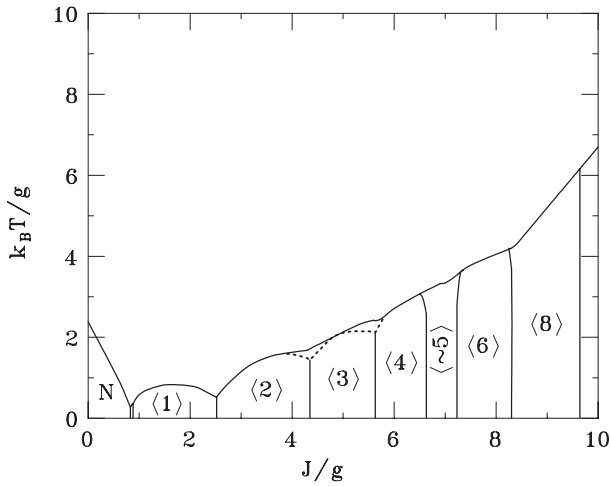


Fig. 10.26. Phase diagram of a SQ lattice with  $L = 48$ . The region between the dotted and continuous line is the region where the modulated phase is expected to occur. The checkerboard phases are restricted to the very narrow region between  $N$  and  $\langle 1 \rangle$  phase.

MC simulation by performing a finite-size scaling analysis on a SQ NN Ising model ( $g = 0$ ): one obtains  $k_B T_c/J = 2.269 \pm 0.001 + (0.76 \pm 0.04)/L$  and  $C_{\max}/(k_B L^2) = (0.493 \pm 0.008) \ln L + (0.20 \pm 0.03)$  in very good agreement with the exact result of Ferdinand and Fisher.<sup>115</sup> Incidentally, the shape of the specific heat of the NN model is indistinguishable from that shown in Fig. 10.25 for  $J/g = 100$ . The checked reliability of the MC simulations for  $g = 0$  gives confidence in the anomalous specific heat behaviour observed for  $J/g < 50$ : a change of the order of the phase transition may occur around  $J/g \simeq 50$ .

In Fig. 10.26, we give the phase diagram as obtained from analytic calculations at  $T = 0$  and MC simulations on a lattice  $48 \times 48$  at finite temperature. The continuous line in Fig. 10.26 was obtained by the location of the specific heat peak characterizing the transition to the tetragonal or paramagnetic phase. The dotted curve is the transition between the stripe and the modulated phase. As one can see, the phase diagram shows a variety of configurations depending on the ratio  $J/g$ . Indeed, for  $J = 0$  (pure dipole interaction), the ground state corresponds to an antiferromagnetic  $N$  configuration. As the ratio  $J/g$  increases, the ground state is characterized by  $\langle 1, n \rangle$  configurations in the narrow range  $0.8304 - 0.8806$  and by the stripe configurations  $\langle 1 \rangle$ ,  $\langle 2 \rangle$ ,  $\langle 3 \rangle$ ,  $\langle 4 \rangle$ ,  $\langle \sim 5 \rangle$ ,  $\langle 6 \rangle$ ,  $\langle 8 \rangle$ ,  $\langle 12 \rangle$ ,  $\langle 24 \rangle$  (the last two not shown in the phase diagram) for  $0.8806 < J/g < 17.27$ . Finally, for  $J/g > 17.27$ , the  $F$  configuration becomes stable. An important difference between the phase diagram shown in Fig. 10.26 and a previous phase diagram<sup>109</sup> obtained for the same model using a much smaller lattice of side  $L = 16$ , is the existence of a modulated phase in proximity of the phase boundary  $\langle 2 \rangle - \langle 3 \rangle$  and  $\langle 3 \rangle - \langle 4 \rangle$ . The strong reduction of the existence region of the modulated phase away from the boundaries and its disappearance in proximity of the boundary  $\langle 1 \rangle - \langle 2 \rangle$  indicate the importance of

using large-size lattices. As for the order–disorder phase transition, we are in favour of the existence of a continuous transition for small  $J/g$  where the ground state is a Néel state and for large  $J/g$  ( $J/g \gtrsim 50$ ) where the ground-state configuration is ferromagnetic. As for the critical exponents, however, the long range dipole–dipole interaction should play an important role. The transition temperature decreases linearly from  $k_B T/g = 2.4$  to 0.4 as  $J/g$  goes from 0 to 0.8. In the narrow region  $0.83 < J/g < 0.88$ , the specific heat shows a sharp peak typical of a first-order phase transition. A multiphase point at  $T = 0$  and  $J/g = 0.8806$  corresponds to the confluence of infinite  $\langle 1, n \rangle$  checkerboard configurations. Around the boundaries  $\langle 2 \rangle - \langle 3 \rangle$  and  $\langle 3 \rangle - \langle 4 \rangle$ , a modulated phase characterized by an incommensurate wavevector  $\mathbf{Q}$  occurs between the stripe and the paramagnetic phase.